An assessment of land energy balance over East Asia from multiple lines of evidence and the roles of Tibet Plateau, aerosols, and clouds

Qiuyan Wang[1,2,6], Hua Zhang[1,2], Su Yang[3], Qi Chen[2], Xixun Zhou[2], Bing Xie[4], Yuying Wang[1], Guangyu Shi[1,5], Martin Wild[6]

[1] Collaborative Innovation Center on Forecast and Evaluation of Meteorological Disasters, Nanjing University of Information Science and Technology, Nanjing 210044, China

[2] State Key Laboratory of Severe Weather, Chinese Academy of Meteorological Sciences, Beijing 100081, China

[3] National Meteorological Information Center, China Meteorological Administration, Beijing 100081, China

[4] Laboratory for Climate Studies of China Meteorological Administration, National Climate Center, Beijing 100081, China

[5] State Key Laboratory of Numerical Modeling for Atmospheric Sciences and Geophysical Fluid Dynamics, Institute of Atmospheric Physics, Chinese Academy of Sciences, Beijing 100029, China

[6] Institute for Atmospheric and Climate Science, ETH Zurich, 8092 Zurich, Switzerland

Corresponding to: Hua Zhang (huazhang@cma.gov.cn)

Abstract. With high emissions of aerosols and the known world's "Third Pole" of the Tibet Plateau (TP) in East Asia, knowledge on the energy budget over this region has been widely concerned. This study first attempts to estimate the present-day land energy balance over East Asia by combining surface and satellite observations, as well as the atmospheric reanalysis and Coupled Model Intercomparison Project phase 6 (CMIP6) simulations. Compared to the global land budget, a substantially larger fraction of atmospheric shortwave radiation of 5.2% is reflected, highly associated with the higher aerosol loadings and more clouds over East Asian land. While a slightly smaller fraction of atmospheric shortwave absorption of 0.6% is unexpectedly estimated, possibly related to the lower water vapor content effects due to the thinner air over the TP to overcompensate for the aerosol and cloud effects over East Asian land. The weaker greenhouse effect and fewer low clouds due to the TP are very likely the causes for the smaller fraction of East Asian-land surface downward longwave radiation. Hence, high aerosol loadings, clouds, and the TP over East Asia play vital roles in the shortwave budgets, while the TP is responsible for the longwave budgets during this regional energy budget assessment. The further obtained cloud radiative effects suggest that the presence of clouds results in a larger cooling effect on the climate system over East Asian land than that over globe. This study provides a perspective to understand fully the roles of potential factors in influencing the different energy budget assessments over regions.

1. Introduction

Current patterns of Earth's weather and climate are largely determined by the spatiotemporal distributions of energy exchanges between the surface, atmosphere, and space. Theoretically, the outgoing longwave radiation (OLR) is balanced by the incoming and reflected solar radiation at the top of the atmosphere (TOA) to produce an equilibrium climate. The incoming solar radiation can be scattered by clouds and aerosols or absorbed by the intermediary atmosphere, thereby contributing to the diverse energy transformation at the surface (Trenberth et al., 2009; Wild et al., 2013a). The Earth's surface energy balance is of particular significance because it is the key driver of atmospheric and oceanic circulations, hydrological cycles, and various surface processes (Wild et al., 2008; Mercado et al., 2009; Wild et al., 2013a; L'Ecuyer et al., 2015). Anthropogenic influences on climate change are driven by the uneven distribution of the TOA net radiation caused by forcings perturbed by variations of the atmospheric composition of greenhouse gases and aerosols as well as aerosol-cloud interactions (Trenberth et al., 2009; Stephens et al., 2012; Wild et al., 2013a; Trenberth et al., 2014; L'Ecuyer et al., 2015; Wild et al., 2019; Z. Wang et al., 2021).

Many efforts have been made to quantify the magnitudes of different radiative components or energy budgets in the climate system over a range of time-space scales, such as on global scales (Lin et al., 2008; Trenberth et al., 2009; Stephens et al., 2012; Wild et al., 2013b; Wild et al., 2015; L'Ecuyer et al., 2015; Wild et al., 2019; Wild, 2020), over land and ocean domains or the energy transport between them (Fasullo and Trenberth, 2008a, b; Trenberth et al., 2009; Wild et al., 2015; L'Ecuyer et al., 2015), over the Arctic (Previdi et al., 2015; Christensen et al., 2016), and over individual continents and ocean basins (L'Ecuyer et al., 2015; Kim and Lee, 2018; Thomas et al., 2020). The energy balance at the TOA can be accurately

monitored by satellites from the most advanced Clouds and the Earth's Radiant Energy System (CERES) Energy Balanced and Filled (EBAF) data product (Loeb et al., 2018), while considerably larger uncertainties appear at the surface fluxes owing to weaker observational constraints (Raschke et al., 2016; Kato et al., 2018; Huang et al., 2019). These assessments mostly build upon complementary approaches from a combination of space and surface observations, climate models, and reanalyses. To date, the discrepancies of independent global mean surface radiative fluxes have estimated to be within a few W m^{-2} (Wild, 2017a, b), enabling the accurate quantification of global surface budgets. In addition, the surface radiative components simulated by various climate models vary substantially in a range of around 10–20 W m^{-2} on global scales, but exhibit greater inter-model discrepancies on regional scales (Li et al., 2013; Wild et al., 2013a; Boeke and Taylor, 2016; Wild et al., 2015; Wild, 2017a, b, 2020). Existing challenges on the surface energy estimates include considerable uncertainties from surface albedo and skin temperature, as well as the partitioning of surface net radiation into sensible and latent heat (SH; LH) (Wild, 2017a, b).

Due to the large population and the largest emission source of aerosols and their precursors, East Asia, especially China, has long been a hotpot in climate change research. Aerosols can interact with radiation directly by scattering and absorbing solar/thermal radiation (Ghan et al., 2012) and indirectly by modifying cloud microphysical properties and lifetimes (Li et al., 2011), thereby influencing Earth's radiation balance. As the world's largest and highest plateau, the Tibet Plateau (TP) covers nearly one fifth of the East Asian land area, significantly affecting the atmospheric circulation, energy budget, and water cycles of climate system through its orographic and thermal effects (Liu et al., 2007; Xu et al., 2008a, b; Wu et al., 2015). Deeper insights into the energy budget differences over East Asian and global land under the background of high aerosol emissions and the role of the TP in East Asia are of the meaningful and essential attempts. Moreover, clouds play a key role in modulating global and regional energy budgets and hydrological cycles through increasing the reflected solar radiation and also the downward thermal radiation, leading to a cooling and warming of climate system (Stephens, 2005; Wild et al., 2013a; Li et al., 2015; H. Wang et al., 2021). Therefore, our emphasis in this study is on the regional characterization of the East Asian energy balance under both all-sky and clear-sky conditions based on a combination of surface observations, satellite-derived products, reanalysis, and Coupled Model Intercomparison Project phase 6 (CMIP6) models. The cloud influence on the radiative energy budgets at the TOA, within the atmosphere, and at the surface is further quantified over this region. Section 2 introduces the different data sources used in this study, including surface and satellite observations, climate models, and reanalysis. Sections 3 and 4 provide detailed analyses of the all-sky and clear-sky estimates of the energy balance components. The inferred cloud radiative effects (CREs) at the TOA, within the atmosphere, and at the surface are presented in Section 5. Summary and conclusions are given in Section 6. The present-day in this study represents years of 2010–2014, which corresponds to the last five years of the historical simulations in CMIP6 climate models. East Asian land as considered in this study consists of five countries, including China, Japan, South and North Korea, as well as Mongolia.

2. Data sources

2.1. Surface observations

Considering the efforts to diminish the inhomogeneities in the measurement of ground-based surface (downward) solar radiation (SSR) (Tang et al., 2011; Wang, 2014; Wang et al., 2015; Wang and Wild, 2016; He et al., 2018; Yang et al., 2018, 2019) and the large amount of observational stations over China, the homogenized monthly all-sky and clear-sky SSR datasets from the China Meteorological Administration (CMA) National Meteorological Information Center (NMIC) are used in this study (http://data.cma.cn/enl) (Yang et al., 2018, 2019). In this dataset, the clear-sky condition at observational sites is defined based on the measured cloud fraction per day of no more than 15% (Yang et al., 2018). Taking clear-sky data (with relatively complex missing months compared to the all-sky dataset) as an example, sites with more than one year of > 2 missing months were deleted to ensure ≥ 4 years of available data during the period 2010-2014, then the spline interpolation was performed on the missing months of the selected sites. As a consequence, 99 and 76 sites are available for the all-sky and clear-sky studies, respectively. Besides, to further explore the anthropogenic influence on SSR, 84 (62) urban and 15 (14) rural stations for all-sky (clear-sky) conditions are defined according to the administrative divisions of China (Wang et al., 2017).

For the remaining East Asian sites, we use the monthly Global Energy Balance Archive (GEBA) dataset (http://www.geba.ethz.ch) (Wild et al., 2017), which contains a worldwide widespread distribution of monthly data from many sources, e.g., from the World Radiation Data Center (WRDC), the Baseline Surface Radiation Network (BSRN), etc. Among these data sources, the BSRN dataset has a much higher precision and temporal resolution (up to 1 min) compared to the GEBA, but its site number is very limited over East Asia (only a few sites located in Japan and one site in Xianghe, China, but with no data available during this study period). Moreover, the relative random error of the monthly SSR from the GEBA data evaluated by Gilgen et al. (1998) is 5%.

In order to retain as many sites as possible during the study period, we widen the selection criterion of the GEBA data, i.e., sites with data ≥ 4 years and missing months ≤ 3. Eventually, 8, 2, 4, and 14 sites are selected from GEBA in China, Mongolia, South and North Korea, and Japan, respectively. Especially, among the 14 sites in Japan, five pairs of the duplicate sites are obtained from the WRDC and BSRN sources, respectively, and the left 4 sites are only from the WRDC (9 sites available). For China, only one site from Hongkong out of 8 GEBA sites is not repetitive from the above-mentioned CMA sites (1 site available). Therefore, 16 out of 28 GEBA sites are available under all-sky conditions (including 15 sites over regions outside China and 1 site over Hongkong, China) by taking the average of these duplicate sites in Japan instead, while the clear-sky reference sites are obtained from the interpolated CERES EBAF clear-sky estimates at the GEBA sites (also 16 sites) due to the limited numbers of observational sites over these regions. Additionally, we regard four island sites in Japan as rural stations (not shown in the figures), while the sites in Mongolia as well as South and North Korea are all urban sites.

130   As shown in Fig. S1, there are 99 (rural/total: 15/99) and 16 (rural/total: 4/16) sites from the CMA and

131   GEBA available under all-sky conditions, respectively, whereas 76 (rural/total: 14/99) and 16 (from the

132   CERES-interpolated data at the 16 GEBA sites) sites are considered for clear-sky conditions, respectively.

133   More detailed station information is given in Table S1.

134

135   ## 2.2.   Satellite observation

136   Owing to the excellent temporal and spatial coverage of satellite instruments, CERES data products are

137   widely used to track variations of Earth's energy budgets. The newly released CERES EBAF Edition 4.1

138   with a monthly $1°×1°$ latitude-longitude resolution is used in this study (https://ceres.larc.nasa.gov/data/). In

139   this dataset, the TOA radiation components are adjusted within their uncertainty ranges based on the

140   independent observational ocean estimates of global heating rate (Loeb et al., 2018). Unlike the directly

141   measured TOA energy budget, the EBAF-surface energy fluxes are calculated by the cloud and aerosol

142   properties from satellite-derived products as well as the atmospheric profiles from reanalysis, with a lower

143   accuracy than their TOA counterparts (Kato et al., 2018). The uncertainty ranges in $1°×1°$ regional monthly

144   all-sky and clear-sky longwave (LW) and shortwave (SW) radiation fluxes at the TOA are also documented

145   by Loeb et al. (2018).

146

147   ## 2.3.   Climate models and reanalysis

148   Data from 40 CMIP6 climate models are used for the analyses in this study with their model

149   abbreviations, modeling groups, and resolutions in Table S2. A detailed description of the modeling groups

150   participating in CMIP6 is provided at https://pcmdi.llnl.gov/CMIP6/. The CMIP6 model-calculated radiation

151   fluxes under investigation for this study include energy budgets under both all-sky and clear-sky conditions

152   from 'historical all forcings' experiments covering the period 2010-2014. In these historical simulations,

153   both natural (e.g., solar variability and volcanic aerosols) and anthropogenic (e.g., greenhouse gases, aerosols,

154   and land use) forcings are considered to reproduce the climate change and evolution since preindustrial times

155   as accurately as possible (Eyring et al., 2016). Only the first ensemble member of each model is selected for

156   the analysis and the model numbers vary slightly among different available energy components.

157   In the long history of the European Center for Medium-range Weather Forecast (ECMWF), ERA5 is

158   the fifth generation product. It is a comprehensive reanalysis from 1959 to near real time, which assimilates

159   as   many   observations   as   possible   in   the   upper   air   and   near   surface

160   (https://cds.climate.copernicus.eu/cdsapp#!/dataset/reanalysis-era5-single-levels-monthly-

161   means?tab=form). Monthly means of the radiative components from ERA5 are used in this study with a

162   resolution of $0.25°×0.25°$ (regridded to $1°×1°$). Compared to previous reanalyses (such as ERA-Interim), a

163   major strength of ERA5 is the much higher temporal and spatial resolutions, as well as a higher vertical

164   resolution with 137 levels (Hersbach et al., 2020). Several independent studies have evaluated the

165   performance of ERA5 since its release. For example, excellent closure of the Arctic energy budget based on

166 ERA5 atmospheric data has been assessed by Mayer et al. (2019). The representation of surface irradiance
167 of ERA5 has been compared with other reanalyses and with ground and satellite observations (Trolliet et al.,
168 2018; Urraca et al., 2018). Specifically, Trolliet et al. (2018) found that the surface solar irradiance over the
169 tropical Atlantic Ocean from ERA5 exhibits fewer biases than the second version of the Modern-Era
170 Retrospective Analysis for Research and Applications (MERRA-2). Urraca et al. (2018) reported that ERA5
171 can be a valid alternative for satellite-derived products in terms of surface irradiance in most inland stations
172 compared to ERA-Interim or MERRA-2. Furthermore, based on BSRN station data, Tang et al. (2021)
173 pointed out that the accuracy of the ERA5 over land in terms of surface downward longwave radiation is
174 higher than CERES-derived product on average both at hourly and monthly times scales.

175

3. Assessment of land energy balance budgets under all-sky conditions

3.1. Shortwave components

178   Under all-sky conditions, the present-day annual land-mean anomalies of TOA incident solar radiation
179 as well as the SW net radiation at the TOA, within the atmosphere, and at the surface regarding to their
180 respective multi-model means as simulated by various CMIP6 models over East Asia are shown in Fig. 1a.
181 A summary of the CMIP6 model statistics (such as available model number, model spread, and the standard
182 deviation (SD)), along with the corresponding multi-model mean, ERA5-, and CERES-derived estimates of
183 different energy balance components are listed in Table 1. As shown in Fig. 1a, with the exception of the
184 BCC-CSM2-MR and BCC-CESM1 models, all models give an estimate around 334 W m^{-2} for TOA
185 incoming solar radiation with a very small SD of 0.2, closely matching the multi-model mean as well as the
186 CERES and ERA5 estimates (Table 1). The multi-model means of solar absorption at the TOA, within the
187 atmosphere, and at the surface are 217, 73, and 144 W m^{-2}, respectively, all within 2 W m^{-2} of the biases
188 against the CERES-derived estimates, while they are 3–4 W m^{-2} larger for those from ERA5 at the TOA and
189 within the atmosphere, yielding 1 W m^{-2} of bias against the CERES-based estimate at the surface (Table 1).
190 However, the individual models vary significantly in their simulated annual East Asian land-mean solar
191 absorption both at the TOA and surface (Fig. 1a), with SDs of around 6 W m^{-2} and inter-model spreads of
192 more than 20 W m^{-2} (Table 1). Considering the smaller absolute amount of atmospheric and surface solar
193 absorption compared to the TOA counterpart (73 and 144 vs. 217 W m^{-2}; Table 1), the relative (percentage)
194 differences relative to their respective multi-model means (relative (percentage) difference =
195 $\frac{\text{range}}{\text{multi-model mean}} \times 100\%$) indicate that the uncertainties within the atmosphere and at the surface are larger
196 than that at the TOA (i.e., TOA: $\frac{22}{217} \times 100\% = 10\%$; Atmosphere: $\frac{19}{73} \times 100\% = 26\%$; Surface:
197 $\frac{23}{144} \times 100\% = 16\%$).

198

199
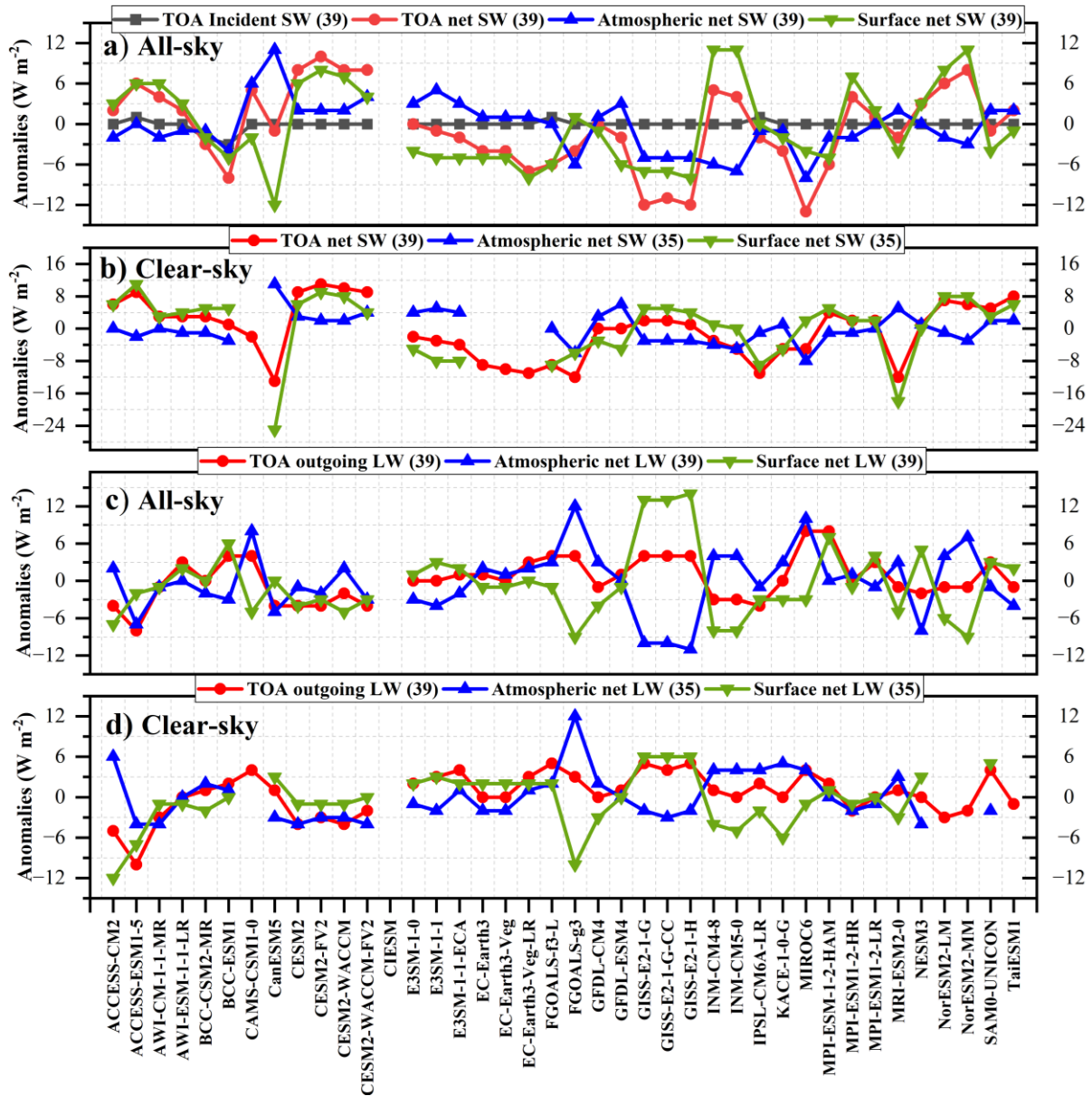
Figure 1. Annual land mean anomalies of (**a**, **b**) shortwave (SW) and (**c**, **d**) longwave (LW) budgets (Units: W m^{-2}) with regard to their respective multi-model means for present-day climate under (**a**, **c**) all-sky and (**b**, **d**) clear-sky conditions over East Asia as simulated by various CMIP6 models. The black, red, blue, and green lines represent the TOA incoming solar radiation, as well as the net SW/LW radiation at the TOA, within the atmosphere, and at the surface, respectively.

205

Table 1. Annual land mean estimates (Units: W m^{-2}) of the magnitudes of various energy balance components and cloud radiative effects (CREs) over East Asia under all-sky and clear-sky conditions at the TOA, within the atmosphere, and at the surface, respectively. The CMIP6 model statistics (e.g., available model number, spread, standard deviation (SD)), as well as the corresponding multi-model mean, ERA5-, and CERES-derived estimates are also given in the Table.

Component (W m^{-2})	CMIP6				ERA5	CERES
	models	spread	SD	mean		
TOA						
Solar down	39	4	0.2	334	334	334
Solar up all-sky	39	23	6	-117	-115	-118

Solar net all-sky	39	22	6.1	217	219	216
Solar up clear-sky	39	24	7	-76	-78	-72
Solar net clear-sky	39	24	6.9	258	256	262
SW CRE	39	26	6.5	-41	-37	-46
Thermal up all-sky	39	12	3.5	-224	-225	-226
Thermal up clear-sky	39	15	3.2	-247	-246	-250
LW CRE	39	12	2.4	23	21	24
Net CRE	39	24	5.8	-18	-16	-22
Atmosphere						
SW absorption all-sky	39	19	3.8	73	78	74
SW absorption clear-sky	35	19	3.8	69	77	71
SW CRE	32	33	6.9	4	2	3
LW net all-sky	39	22	5.1	-152	-150	-157
LW net clear-sky	35	16	3.6	-151	-151	-154
LW CRE	32	14	3.3	-2	1	-3
Net CRE	32	35	7.8	1	2	0
Surface						
SW down all-sky	39	33	7.6	186	191	178
SW up all-sky	39	24	6.5	-43	-50	-36
SW absorbed all-sky	39	23	6.1	144	141	142
SW down clear-sky	35	25	4.6	242	238	236
SW up clear-sky	35	27	6.8	-53	-59	-45
SW absorbed clear-sky	32	36	7.8	189	179	191
SW CRE	35	28	6.6	-46	-38	-49
LW down all-sky	39	27	7.9	280	273	285
LW up all-sky	39	23	7.1	-352	-347	-354
LW net all-sky	39	23	5.7	-71	-74	-69
LW down clear-sky	35	26	6.8	256	253	256
LW up clear-sky	35	23	7.1	-351	-347	-353
LW net clear-sky	35	18	4.1	-95	-94	-97
LW CRE	35	12	3.5	24	20	27
net CRE	32	31	6	-21	-18	-22
net radiation	39	20	5.3	72	67	73
LH	40	26	4.7	-43	-38	—
SH	40	21	5.2	-31	-29	—

211

The simulated SSR, however, shows the largest spread of more than 30 W m^{-2} (ranging from 172–205 W m^{-2}) among all the substantially differing all-sky surface radiation components, with a large SD of 7.6 W m^{-2} (Fig. 2a; Table 1). The multi-model mean SSR is estimated to be 186 W m^{-2}, suggesting positive and negative deviations of 8 and 5 W m^{-2} from the CERES- and ERA5- derived estimates, respectively (Table 1). Interestingly, although the discrepancy between them is very large (8 or 5 W m^{-2}), both the resulting surface solar absorption differences are very small (within 3 W m^{-2}), indicating that a higher SSR goes together with a higher surface albedo (Table 1), which agrees well with that on a global mean level (Wild et al., 2015).

220
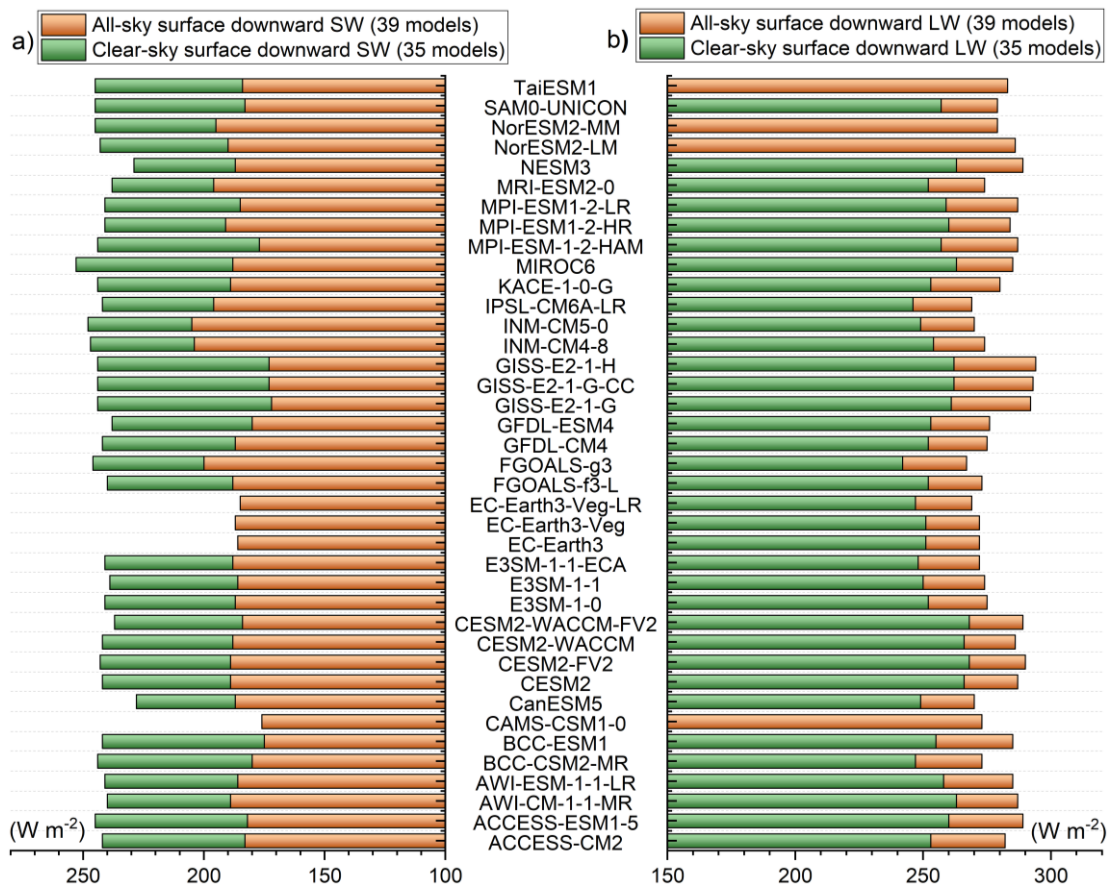
Figure 2. Annual land mean surface downward (**a**) SW and (**b**) LW radiation (Units: W m^{-2}) under both all-sky (orange bars) and clear-sky (green bars) conditions over East Asia as calculated by various CMIP6 models.

3.2. Best estimates for the surface downward SW radiation

As a major component of Earth's energy balance, the solar radiation reaching the Earth's surface governs a wide range of surface physical and chemical processes. The spatial distributions of the site-based annual mean SSR from the CMA and GEBA (Section 2.1) over East Asia under all-sky conditions are presented in Fig. 3a, together with the classified rural and urban sites. In short, the high values are mainly located at the high elevation stations over western China and a few island sites in Japan (e.g., Minamitorishima, Japan; not shown in the figure), especially over the TP, with the largest value reaching 263 W m^{-2} (Geer, Tibet), which is associated with the high atmospheric transparency over these regions. However, the low annual mean values are primary over southwestern China, with the smallest value of 103 W m^{-2} (Shapingba, Chongqing), which is possibly caused by the higher aerosol loadings (Liao et al., 2015; de Leeuw et al., 2018) and more clouds (Li et al., 2017; You et al., 2019; Lei et al., 2020; Zhang et al., 2020) over these regions. This distribution pattern is highly consistent with that over China documented by Q. Wang et al. (2021).
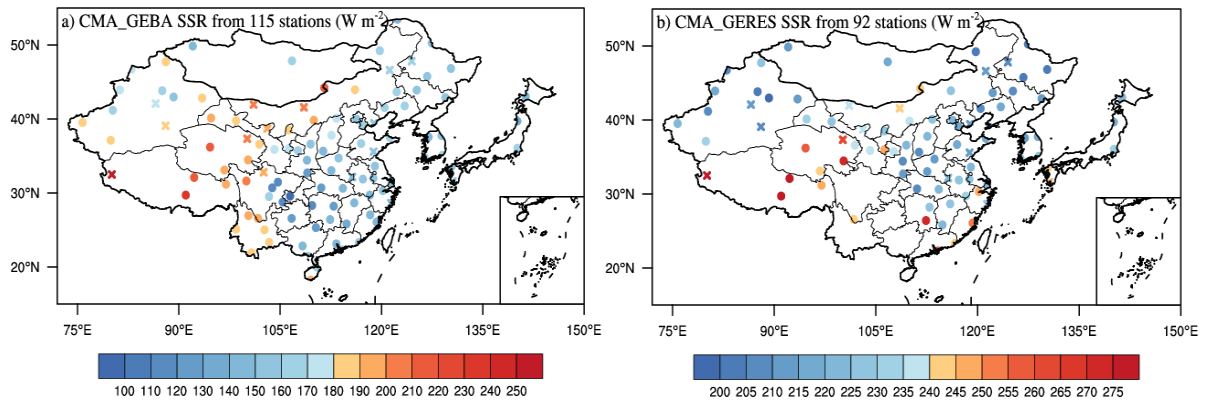
Figure 3. Spatial distributions of annual mean surface downward solar radiation (SSR) (Units: W m⁻²) under (**a**) all-sky and (**b**) clear-sky conditions over East Asia. The all-sky sites are available from 99 CMA and 16 GEBA stations, while there are 76 CMA and 16 CERES-interpolated sites for clear-sky conditions. The cross and circle symbols indicate rural (19 vs. 18 for all-sky and clear-sky conditions) and urban stations (96 vs. 74), respectively.

Figure 4 shows the distributions of annual mean SSR biases derived from the CERES, CMIP6 multi-model mean, and ERA5 against the surface observations, as well as the comparisons of their respective annual land means at the surface sites with their observed counterparts. The corresponding quantifications of the magnitudes of station-mean biases are also given in Table 2. According to the comparisons, they all correlate well with the ground-based observations, with their respective high correlation coefficients of 0.93, 0.87, and 0.89, indicative of the highest accuracy in the CERES-derived estimate (Figs. 4b, d, and f). To quantify their SSR mean biases against the corresponding observed counterparts, the CERES-based bias at all sites is the smallest, with a station-mean bias of 3.8 W m⁻², followed by the CMIP6 multi-model mean and the ERA5 reanalysis (with respective station-mean biases of 13.8 and 16.5 W m⁻²) (Table 2). Additionally, among all the aforementioned SSR estimates, the East Asian urban sites are in general more significantly overestimated than the rural sites on average compared to the surface observations (Figs. 4b, d, and f; Table 2). This further supports the argument that rural stations might be more representative for larger scale comparisons (e.g., the general circulation model grid scales) than the urban stations (which are vulnerable to local pollution) (Wang et al., 2018). The overestimations are mainly located in the high-latitude regions over East Asia for CERES-derived estimates (among them the underestimations mostly from rural sites), while the underestimates are primarily located in lower-latitude and eastern coastal regions (Figs. 4a and b). The CMIP6 multi-model mean and ERA5-derived SSR generally greatly overestimate the surface-based observations both at urban and rural sites, except for the regions over northern and northeastern Inner Mongolia, northwestern Heilongjiang (located in the northeastern China), and some individual sites over southwestern China (Figs. 4c-f). The annual land-mean area-weighted average SSR over East Asia derived from CERES is estimated to be 178 W m⁻², which is closest to the surface observational estimate of 174 W m⁻², compared to the much higher overestimations of both the CMIP6 multi-model mean and ERA5 (186 and 191W m⁻²) against the surface observations (Table 3), which shows a high consistency with their bias distributions and the collocated quantifications (Fig. 4; Table 2).

272
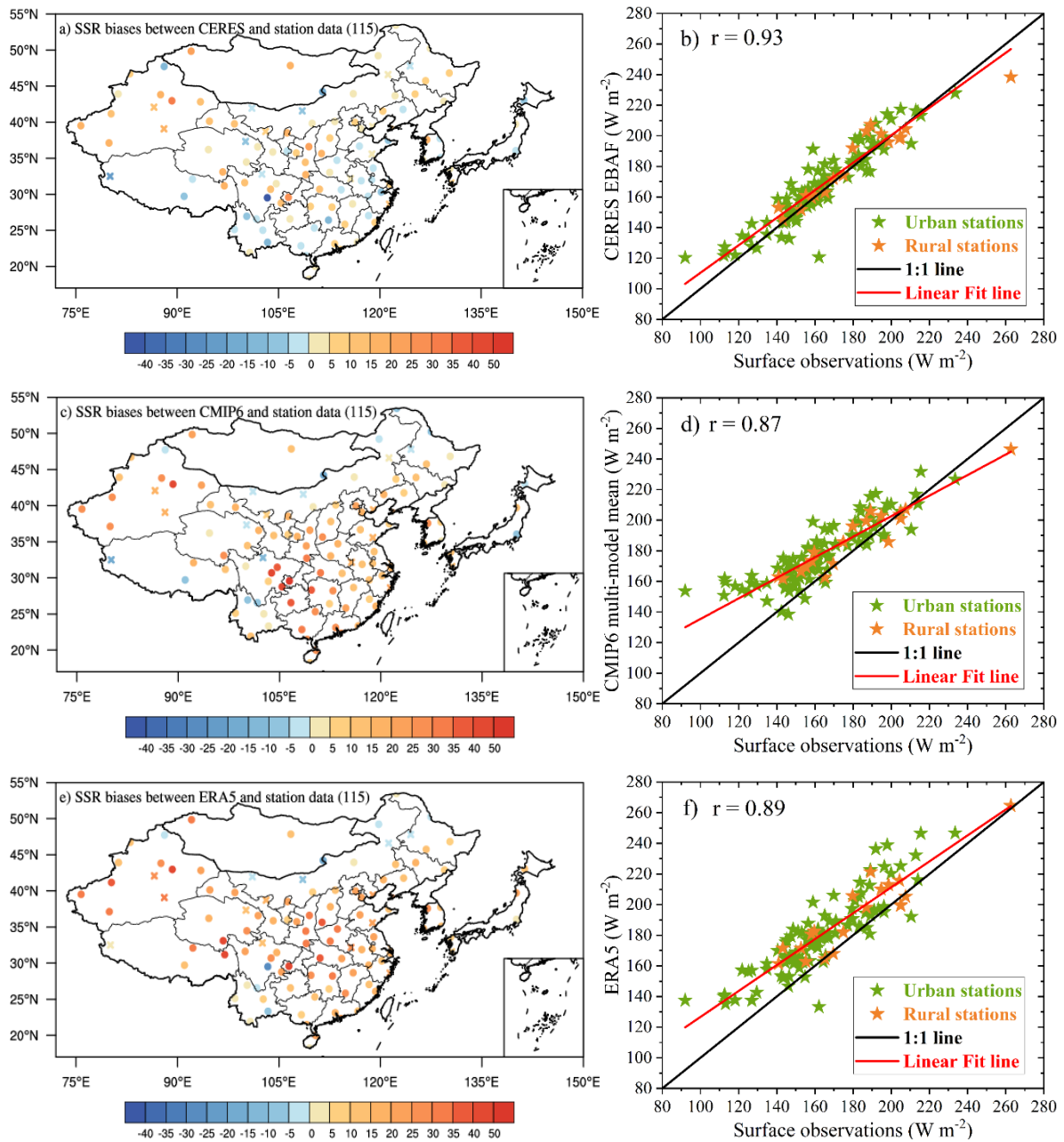
Figure 4. Spatial distributions of annual mean SSR biases (Units: W m^{-2}) derived from (**a**) CERES-EBAF,
(**c**) CMIP6 multi-model mean, and (**e**) ERA5 reanalysis at a combination of the CMA and GEBA sites under
all-sky conditions over East Asia. The corresponding comparisons of their respective annual means at the
surface sites with their observed counterparts are displayed in (**b**), (**d**), and (**f**), respectively. The cross and
circle symbols in Figs. **a, c, e** as well as the orange and green stars in Figs. **b, d, f** indicate rural and urban
stations, respectively.

Table 2. Annual station-mean SSR biases (Units: W m^{-2}) derived from CERES-EBAF, CMIP6 multi-model
mean, and ERA5 compared to the surface observational sites under all-sky and clear-sky conditions during
2010-2014 over East Asian land, together with the separate station averages of biases at urban and rural sites.
The values in parentheses represent the percentages of SSR biases relative to their respective station-mean
averages with the largest percentages around 10% and 4% for all-sky and clear-sky conditions.

Station-mean SSR biases	All-sky			Clear-sky		

(Unit: W m^{-2})	all	urban	rural	all	urban	rural
CERES-EBAF	3.8 (2.3%)	4.2 (2.6%)	1.7 (0.9%)	0.4 (0.2%)	0.5 (0.2%)	-0.3 (-0.1%)
CMIP6	13.8 (8.3%)	15 (9.2%)	7.4 (4.1%)	9.1 (4%)	9.7 (4.3%)	6.4 (2.8%)
ERA5	16.5 (10%)	17.2 (10.5%)	12.7 (7%)	5.7 (2.5%)	6.2 (2.7%)	3.6 (1.5%)

285

286 **Table 3.** Annual land mean area-weighted average SSR (Units: W m^{-2}) from a combination of the CMA and
287 GEBA (CERES-interpolated) site observations under all-sky (clear-sky) conditions during the period 2010-
288 2014 over East Asia, together with the corresponding estimates from the CERES-EBAF, CMIP6 multi-
289 model means, and ERA5, respectively.

Average annual mean SSR during 2010-2014 over East Asia (Units: W m^{-2})	Surface observations	CERES-EBAF	CMIP6	ERA5
All-sky	174	178	186	191
Clear-sky	230	236	242	238

290

291   However, the ground-based observations are spatially limited with sparse stations in some remote
292 regions and are thus inadequate for many applications, as they may be not representative for real situations.
293 To better constrain the large spread in the model-based SSR outlined above, we combine the ground-based
294 observations to obtain the best estimate referring to the approach introduced in Wild et al. (2013a). Figure
295 5a gives various CMIP6 model biases of all-sky SSR at all the surface sites and their respective East Asian
296 land means. The higher overestimations relative to surface observations generally correspond to higher
297 model-based East Asian land means, with a much higher correlation coefficient of 0.96 than that of 0.88 on
298 the global scale (Wild et al., 2015). Thus, the best estimate of the annual East Asian land-mean SSR is
299 deduced to be 174.2±1.3 W m^{-2} (2σ uncertainty) in light of the linear regression analysis. The corresponding
300 estimates from CERES and ERA5 are also labeled in the figure, at 178 and 191 W m^{-2}, respectively, implying
301 a slight and substantial overestimation for CERES and ERA5 estimates. There is an overall tendency that
302 most models overestimate the surface downward SW fluxes (36 out of 39 sites) compared to the ground-
303 based observations, with a multi-model mean overestimation relative to site observations of 13.8 W m^{-2},
304 which is also a longstanding issue in climate modelling (Wild et al., 1995; Wild et al., 2015).

305
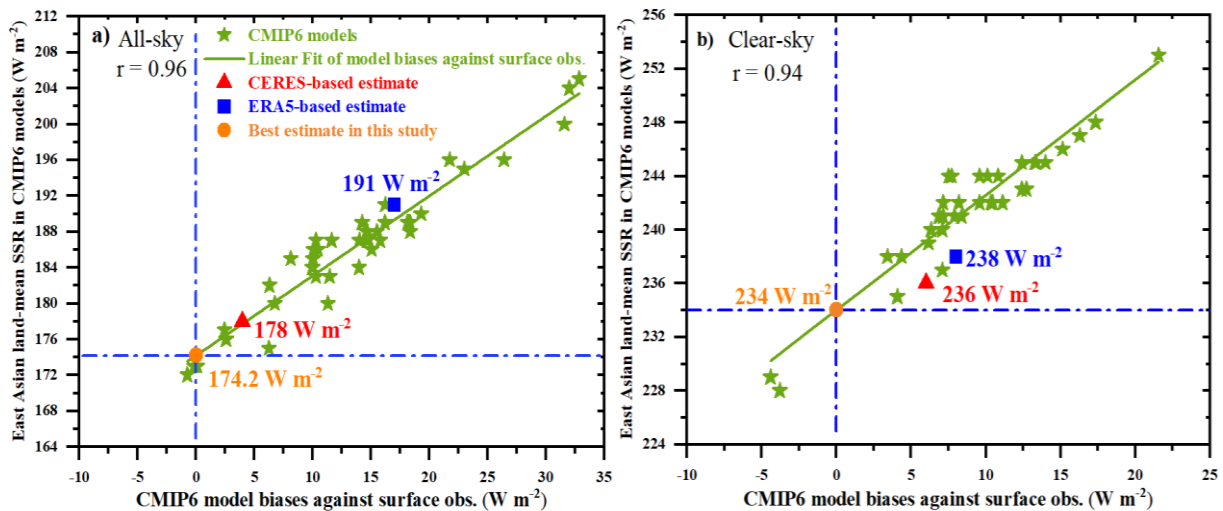
306

307 **Figure 5.** Annual land mean SSR (Units: W m^{-2}) of various CMIP6 models as well as their respective model
308 biases relative to an average over surface sites (99 CMA and 16 GEBA for all-sky; 76 CMA and 16 CERES-
309 interpolated sites for clear-sky) under (**a**) all-sky and (**b**) clear-sky conditions during 2010-2014 over East
310 Asia. Green stars represent various CMIP6 models. Best estimate here (orange circle) can be inferred from
311 the intersection between the linear regression line (green solid lines) and the zero-bias line (blue dotted lines).
312 Furthermore, the corresponding estimates from CERES-EBAF and ERA5 are also given by red triangle and
313 blue square, respectively.

314

315 3.3. Longwave components

316   Similar to the all-sky SW counterparts, obvious discrepancies can still be noted in the annual land-mean

317 LW radiation over East Asia among models, especially for those within the atmosphere and at the surface

318 (Fig. 1c). Correspondingly, the simulated TOA OLR varies in a range of 12 W m^{-2}, which is almost 10 W

319 m^{-2} lower than that within the atmosphere (22 W m^{-2}) and at the surface (23 W m^{-2}) (Table 1). The estimated

320 annual East Asian land-mean TOA OLR from the CMIP6 multi-model mean is -224 W m^{-2}, within 2 W m^{-2}

321 of the deviations from the CERES- and ERA5-inferred estimates. The model spread of the simulated annual

322 land-mean net LW radiation becomes larger from the TOA to the surface, with SDs of 3.5, 5.1, and 5.7 W

323 m^{-2}, respectively, which shows the same tendency as the relative (percentages) differences with respect to

324 their multi-model means (5.4%, 14.5%, and 32.4%).

325   These large discrepancies in surface net LW radiation between models are particularly evident in the

326 surface downward LW radiation (Fig. 2b; Table 1), with a range up to 27 W m^{-2} (from 267 to 294 W m^{-2})

327 and a SD of 7.9 W m^{-2}, which is also the largest deviation among all components under all-sky conditions.

328 Compared to the CERES estimates, the slightly lower surface upward LW radiation (-352 vs. -354 W m^{-2})

329 and much lower surface downward LW radiation (280 vs. 285 W m^{-2}) from the multi-model means are the

330 major reason for the small deviation (within 2 W m^{-2}) of the surface net LW radiation between them (Table

331 1). It's interesting to note that the annual East Asian land-mean surface upward LW radiation estimated from

332 the ERA5 is the lowest among all these estimates, at -347 W m^{-2}, suggesting the lowest surface skin

333 temperature of the ERA5 product according to the Stefan-Boltzmann law, followed by the estimates from

334 the multi-model mean and CERES (Table 1). In addition, the annual land-mean surface downward LW

335 radiation estimated by ERA5 is 273 W m^{-2}, approximately 7 and 12 W m^{-2} lower than the estimates by the

336 CMIP6 multi-model mean and CERES, respectively (Table 1). Therefore, both the lower surface upward

337 and downward LW radiation fluxes result in the small deviation in the estimated surface net LW radiation

338 from ERA5 compared to those from the multi-model mean and CERES (Table 1). Since the reanalysis

339 products take as many observed atmospheric parameters with global coverage as possible into consideration

340 during the radiative transfer calculations, they are widely used to obtain more accurate surface LW radiation

341 (Simmons et al., 2004; Wild et al., 2015). We also examined the corresponding surface LW fluxes from

342 another reanalysis, namely MERRA-2, and found much lower annual land means than those from ERA5, in

343 particular for the surface downward LW radiation (not shown), which arrives at the similar conclusions with

344 that documented by Urraca et al. (2018). Thus, considering the limited observational surface LW radiation

345 data over East Asia, ERA5 might be the best reference for the estimates of the annual land-mean surface

346 upward and downward LW radiation, at -347 and 273 W m^{-2}, respectively (Table 1).

347

3.4. Discussion of land energy balance over East Asia under all-sky conditions

3.4.1. Radiative components

Figure 6a displays the schematic diagram of the all-sky land mean energy balance over East Asia, including the above-mentioned SW and LW radiation budgets and other radiative components discussed in the following. The estimated annual East Asian land-mean incoming, reflected, and net SW radiation as well as the OLR at the TOA are therefore 334, -118, 216, and -226 W m^{-2} (Table 1), respectively, based on the CERES EBAF dataset. The corresponding uncertainties are obtained from the uncertainty of 2.5 (1σ uncertainty) W m^{-2} for both SW and LW fluxes given by (Loeb et al., 2018). The annual East Asian land-mean TOA OLR in CERES-EBAF is estimated to be 10 W m^{-2} larger than the TOA absorbed SW radiation, implying an energy loss of 10 W m^{-2} at the TOA under all-sky conditions, which should be compensated by the LH and SH transported from regions outside East Asia (Fig. 6a).

359

360

361
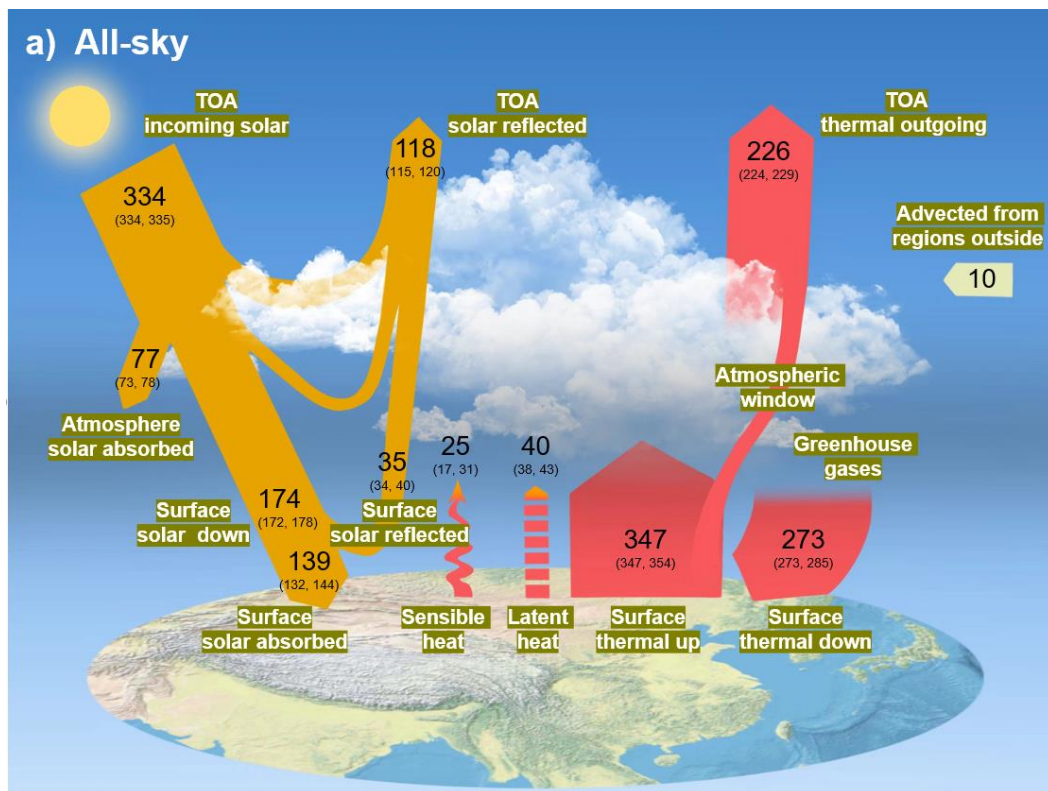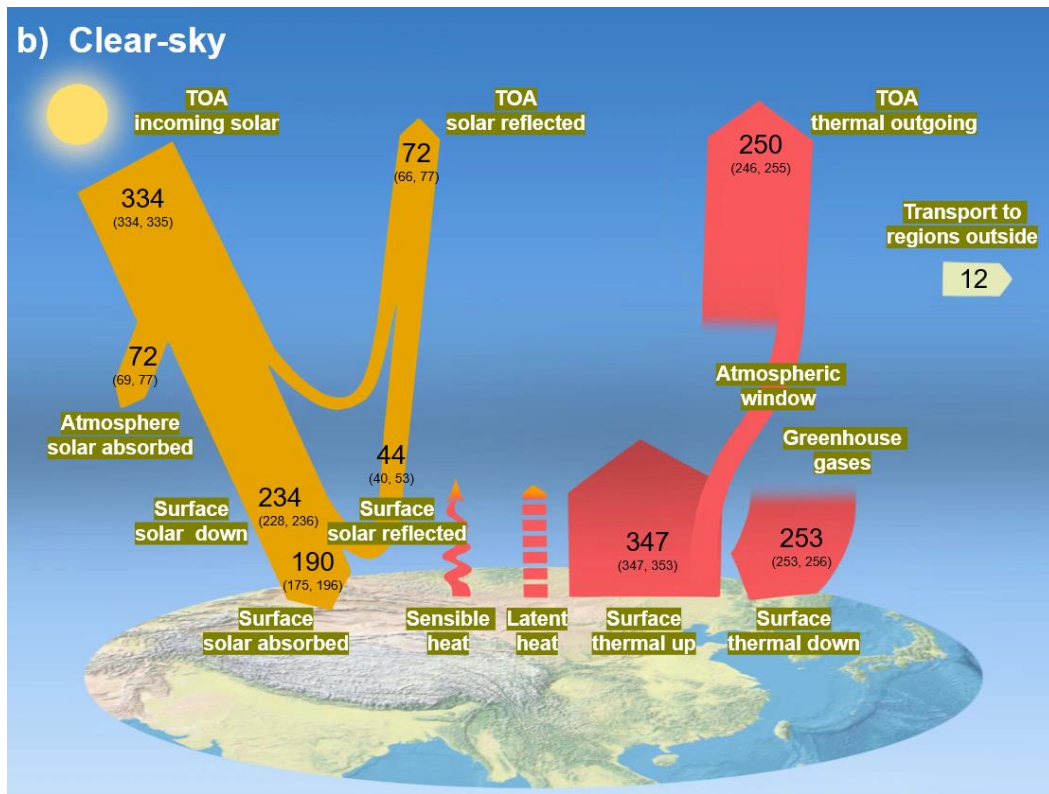
Figure 6. Diagrams of the annual land mean energy balance (Units: W m^{-2}) over East Asia under (**a**) all-sky and (**b**) clear-sky conditions for present-day climate. The uncertainty ranges are also given in parentheses.

For the SSR, the annual East Asian land-mean best estimate based on the CMIP6 multi-model simulations and surface observations is 174.2 W m^{-2} (Fig. 5a and Fig. 6a). Considering the abnormally high overestimation by ERA5 compared to surface observation, the high value of the uncertainty range is given by the estimate from CERES EBAF (178 W m^{-2}), while its low value is from the lowest model estimate (172 W m^{-2}; Fig. 2a) (Fig. 6a). The all-sky surface albedo information is derived from the ratio between the CERES-derived surface upward and downward solar radiation, with a radiation weighted average of around 0.2 (36.4/178.3) over East Asian land. However, the corresponding surface albedos estimated by the CMIP6 multi-model mean and ERA5 are substantially higher than that from the CERES, with respective averages of around 0.23 (42.7/186.4) and 0.26 (49.6/191). Considering the large spatial coverage of remote sensing measurement to map albedo globally, the CERES-derived annual East Asian land-mean surface albedo is adopted as the best estimate in this study. Therefore, considering the rounded best SSR estimate of 174 W m^{-2}, the calculated surface reflected and absorbed SW radiation fluxes are around -35 and 139 W m^{-2}, respectively. As shown in Table 1, the uncertainty range of the surface absorbed SW radiation is 132–144 W m^{-2} according to the lowest value of CMIP6 models and the highest estimate among the aforementioned estimates, which gives rise to an uncertainty range of the surface reflected solar radiation of 34–40 W m^{-2}. Together with the annual East Asian land-mean SW absorption at the TOA and surface of 216 and 139 W m^{-2}, the best estimate for the atmospheric SW absorption is therefore to be 77 W m^{-2}, which is within 4 W m^{-2} of the differences between those estimated from the CMIP6 multi-model mean and CERES and closes

384   to the ERA5-derived estimate of 78 W m^{-2} (Table 1). The uncertainty range of the atmospheric SW

385   absorption is also determined by the estimates from different data sources as shown in Fig. 6a.

386   The downward LW radiation emitted by the atmosphere is mainly sensitive to the near-surface

387   temperature, water vapor, and cloud properties, while the surface emission is in proportion to the skin

388   temperature according to the Stefan-Boltzmann law. As analyzed in section 3.3, the best estimates of the

389   East Asian annual land-mean surface upward and downward LW radiation amount to -347 and 273 W m^{-2},

390   respectively, with uncertainty ranges coming also from the above-discussed different data sources (Fig. 6a).

391   The surface net LW radiation is then estimated to be -74 W m^{-2} based on the surface upward and downward

392   LW radiation outlined above. Combined with TOA outgoing thermal radiation of -226 W m^{-2}, the estimated

393   atmospheric net LW radiation is -152 W m^{-2}, which is close to the collocated estimates from the multi-model

394   mean (-152 W m^{-2}) and ERA5 (-150 W m^{-2}) but deviates substantially from the CERES-derived estimate of

395   -157 W m^{-2} (Table 1). Considering the surface absorbed SW radiation of 139 W m^{-2}, a best estimate for

396   surface net radiation is 65 W m^{-2}, suggesting that around 65 W m^{-2} of energy is available for the non-radiative

397   SH and LH. Besides, the ERA5 estimate of 67 W m^{-2} is very close to the best estimate of 65 W m^{-2}, while

398   much higher estimates of 72 and 73 W m^{-2} are obtained from the multi-model mean and CERES (Table 1),

399   respectively.

400

401   3.4.2.   Nonradiative components

402   The surface net radiation is mainly balanced by the non-radiative components of SH and LH in addition

403   to a very small proportion of ground heat flux and melt (less than 1%) (Ohmura, 2004). However, due to the

404   lack of constraints from in-situ and space observations, this partitioning of the surface net radiation into SH

405   and LH is still subject to considerable uncertainties. As shown in Fig. S2, the simulated annual East Asian

406   land-mean LH and SH vary greatly between different models, with a range of 26 and 21 W m^{-2}, respectively,

407   as well as the relative discrepancies relative to their respective multi-model means of 60% ($\frac{26}{43} \times 100\%$) and

408   68% ($\frac{21}{31} \times 100\%$), respectively, showing larger discrepancies between models with larger uncertainties in SH

409   (Table 1). The best SH estimate can therefore be obtained from the residual of the LH. To obtain a more

410   accurate surface LH from available datasets of the multi-model mean and ERA5, we take an average of them

411   as the best estimate, namely -40 W m^{-2}, the uncertainty ranges of which are also given according to these

412   estimates (Fig. 6a). Note that all the values in this study are calculated on the basis of one decimal point,

413   which may result in 1 W m^{-2} of bias during the rounding process. Combined with the surface net radiation

414   and LH of 65 and -40 W m^{-2}, respectively, the surface SH is estimated to be -25 W m^{-2}, the uncertainty range

415   of which is also given by the existing estimates from various CMIP6 models and ERA5 (Fig. 6a). In addition,

416   although the annual land-mean SH estimated from the MERRA-2 is much higher than the estimates from

417   multi-model mean and ERA5 (not shown), the estimated LH is around -39 W m^{-2} (not shown), very close to

418   the best estimate of -40 W m^{-2}, which increases our confidence in the estimation of this quantity.

419

420 3.4.3.   Comparisons with global annual land-mean estimates

421   Notable discrepancies exist in the global land-mean energy budgets reported by Wild et al. (2015) and
422 the regional land-mean estimates over East Asia in this study (Fig. S3; Table 4). For the SW budgets, the
423 estimated annual land-mean TOA incident solar radiation over East Asia is 9 W m^{-2} higher than that over
424 global land (334 vs. 325 W m^{-2}), implying a slightly lower land-mean solar zenith angle over East Asia.
425 Comparisons also show a slightly higher relative percentage of TOA reflected solar radiation of 0.8% despite
426 of the much lower surface reflected SW radiation of 4.3% over East Asian land compared to global land with
427 respect to their respective TOA incident solar radiation (thereafter call 'relative percentage' for short). This
428 suggests much more relative atmospheric SW reflection of 5.2% over East Asian land, which agrees fairly
429 well with more aerosols (Wei et al., 2019) and more clouds (King et al., 2013; Fan et al., 2018; also see Fig.
430 S4) over this region compared to global land. However, the annual land-mean solar radiation reaching the
431 East Asian surface is around 10 W m^{-2} lower than that over global land (174 vs. 184 W m^{-2}), approximately
432 accounting for 52.1% and 56.6% of their respective incident solar radiation at the TOA, respectively,
433 indicating lower fraction of solar energy arriving at the East Asian surface compared to global land. Together
434 with the lower annual land-mean surface albedo over East Asian land compared to global land (20% vs.
435 26%), this leads to the similar relative percentages of surface absorptions (41.6% vs. 41.9%). Although the
436 magnitude of the atmospheric SW absorptions over East Asian and global land are nearly the same (both
437 around 77 W m^{-2}), the corresponding relative percentage over East Asian land is a little bit lower than that
438 over global land (around 0.6%). This is somewhat unexpected due to the fact of more clouds and aerosol
439 loadings over East Asian land, which is possibly offset by the lower water vapor contents caused by the
440 higher altitudes and thinner air over the TP.

441

442 **Table 4.** Comparisons of the annual mean SW/LW energy balance components (Units: W m^{-2}) over East
443 Asian land (this study) and global land (Wild et al., 2015) as well as the corresponding relative percentages
444 with regard to their respective TOA incident solar radiation/surface LW emissions, along with the relative
445 percentage differences between them.

Component	East Asian land		Global land		Percentage difference
	Annual mean	Relative percentage	Annual mean	Relative percentage	
SW budget					
TOA solar down	334	1	325	1	—
TOA solar up	-118	35.3%	-112	34.5%	0.8%
Atmospheric SW absorption	77	23.1%	77	23.7%	-0.6%
Atmospheric SW reflection	-83	24.9%	-64	19.7%	5.2%
Surface solar down	174	52.1%	184	56.6%	-4.5%
Surface solar up	-35	10.5%	-48	14.8%	-4.3%
Surface solar absorption	139	41.6%	136	41.9%	-0.3%
LW budget					
TOA LW up	-226	65.1%	-232	62.4%	2.7%
Atmospheric LW absorption	-152	43.8%	-166	44.6%	-0.8%
surface LW down	273	78.7%	306	82.3%	-3.6%
Surface LW up	-347	1	-372	1	—

446

447   For the LW budgets, the regional surface LW emission over East Asia is estimated to be much lower

448   than the global land-mean estimates in Wild et al. (2015) (Fig. S3), which mainly results from the lower

449   temperature over the TP induced by high altitudes. The relative percentage of land mean surface downward

450   LW radiation with respect to the surface emission over East Asia is about 78.7 %, which is lower than the

451   global estimate of 82.3%, corresponding well to a reduction in greenhouse effect and fewer low clouds due

452   to the TP (Fig. S4) considering its coverage over East Asian land. Ultimately, a higher percentage of LW

453   radiation is emitted to space over East Asian land compared to global land (65.1% vs. 62.4%). Our estimates

454   also indicate approximately similar amounts of LH (40 vs. 38 W m^{-2}) and much lower SH (25 vs. 32 W m^{-2}

455   ) over East Asia compared to the global land-mean estimates (Fig. S3), which is possibly related to the

456   lower East Asian-land surface temperature.

457   In general, as can be concluded from Table 4, although much less surface SW radiation of 4.3% is

458   reflected over East Asian land compared to global land, a slightly more SW reflection of 0.8% is estimated

459   at the TOA, indicating much larger atmospheric SW reflection of 5.2% due to the stronger scattering from

460   aerosols and clouds over East Asian land than global land. However, the SW absorption within the

461   atmosphere over East Asian land is 0.6% lower than that over global land despite of the more absorption

462   from clouds and aerosols, which is possibly offset by the lower water vapor contents caused by the thinner

463   air over the TP. The lower surface temperature, weaker greenhouse effect and fewer low clouds due to the

464   high altitudes and the thinner air over the TP in East Asian land are the major reasons for the relative lower

465   surface LW emission, less and more fractions of surface downward LW radiation of 3.6% and the OLR of

466   2.7% over East Asian land compared to global land, respectively.

467

4. Assessment of land energy balance budgets under clear-sky conditions

469   The clear-sky land energy balance budgets over East Asia are similarly evaluated as all-sky conditions.

470   Detailed analyses are given in Supplemental material if interested. The annual land-mean SW clear-sky

471   absorptions at the TOA and surface over East Asia show larger variations among different models than that

472   under all-sky conditions (Fig. 1a and b; Table 1), which is consistent with that reported by Wild et al. (2019)

473   but is amazingly in contrast to the recognition that the representation of clouds is the largest uncertainties in

474   climate models (Dolinar et al., 2015). Specially, the surface SW clear-sky absorptions simulated by various

475   models still exhibit a larger uncertainty than the TOA counterparts despite of the lower absolute values (Fig.

476   1b; Table 1). Contrary to the all-sky counterparts, the simulated clear-sky SSR among different models,

477   shows notably smaller inter-model spread and SD than the surface SW absorptions (Table 1), with much

478   smaller model discrepancy compared to the all-sky conditions (Fig. 2a; Table 1).

479   To further constrain the outlined inter-model discrepancy of the simulated clear-sky SSR, surface

480   observations from the CMA and CERES-interpolated estimates at the GEBA sites are utilized in this study.

481   The high values of the station-based clear-sky SSR are mainly located in the TP, but with an abnormally

482   high value located at the southern China (Fig. 3b). All the East Asian land-mean clear-sky SSR estimates

483   from CERES, CMIP6 multi-model mean, and ERA5 agree reasonably well with the surface observations,

484   but with smaller correlation coefficients ranging from 0.78 to 0.82 compared to the all-sky conditions (Figs.

485   7 b, d, and f). The CERES-derived clear-sky SSR is mainly overestimated in central and western China, but

486   with slight underestimations mainly located in northeastern, eastern, and southern China (Fig. 7a). Similar

487   bias patterns can also be found in the clear-sky SSR from the CMIP6 multi-model mean and ERA5 compared

488   to the surface observations, except for some individual sites over northeastern Inner Mongolia, eastern China,

489   western Mongolia, and Japan (Figs. 7c and e), but with relatively smaller overestimations than the all-sky

490   counterparts (Figs. 4c and e; Table 2). Specifically, the smallest station mean bias in CERES-derived SSR

491   compared to the multi-model mean and ERA5 (Table 2) can be attributed to its even distributed surface sites

492   of overestimations and underestimations (Figs. 7b, d, f). Again, among all the aforementioned clear-sky SSR

493   biases, more overestimations exist in urban stations than the rural stations (b, d, f in Figs. 4 and 7; Table 2).

494   Consequently, all East Asian land-mean area-weighted averages of clear-sky SSR from CERES, CMIP6

495   multi-model mean, and ERA5 show higher overestimations of around 6, 12, and 8 W m^{-2}, respectively,

496   compared to the surface observed counterpart of 230 W m^{-2} (Table 3). Based on the similar method

497   introduced in Wild et al. (2015), the best estimate for the East Asian land-mean clear-sky SSR is determined

498   to be 234±1.1 W m^{-2} (2σ uncertainty), with a slightly smaller correlation coefficient of 0.94 and smaller

499   deviations from the CERES and ERA5 estimates compared to the all-sky counterparts (Fig. 5b; Table 3).

500   Besides, the overestimations still exist in the observed land-mean clear-sky SSR for most climate models

501   over East Asia, with a smaller multi-model mean overestimation of 9.1 W m^{-2} than the all-sky counterparts.

502

503
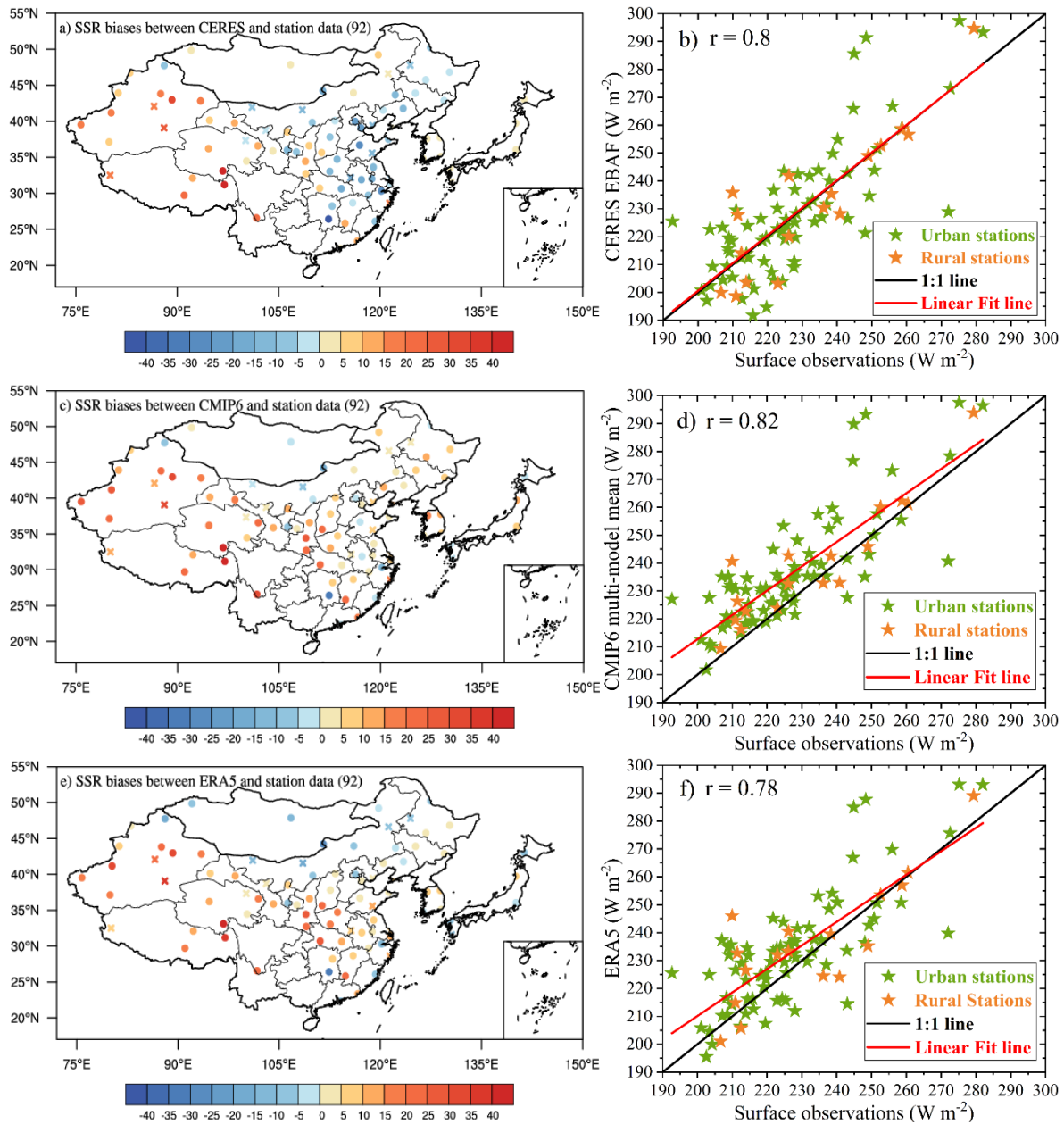
Figure 7. Spatial distributions of annual mean SSR biases derived from (**a**) CERES-EBAF, (**b**) CMIP6
multi-model mean, and (**c**) ERA5 reanalysis against surface observations from a combination of the CMA
and CERES-interpolated sites under clear-sky conditions over East Asia. The corresponding comparisons of
their respective annual land means at the surface sites with their observed counterparts are displayed in (**b**),
(**d**), and (**f**), respectively. The cross and circle symbols in Figs. **a, c, e** as well as the orange and green stars
in Figs. **b, d, f** indicate rural and urban stations, respectively.

510

This clear-sky energy budget only represents the removal of cloud but maintains the same atmospheric
conditions as the all-sky conditions, which is not balanced because it is not the equilibrium state the Earth
would achieve when no clouds could form. Ultimately, the clear-sky East Asian land-mean energy budget is
not closed and with no quantifications of SH and LH as displayed in Fig. 6b. In addition to the analyses
above, the clear-sky TOA energy budgets are derived from CERES-derived product, with uncertainty ranges
referred to Loeb et al. (2018), while the surface LW budgets are again from ERA5 reanalysis. Also,

additional clear-sky radiation weighted surface albedo of 0.19 from CERES is obtained to estimate the surface reflected and absorbed SW radiation. Apart from the TOA budget, all the rest uncertainty ranges are given by different data sources from various CMIP6 models, as well as the multi-model mean, CERES-, and ERA5-derived estimates.

We doublecheck the energy balance components evaluated in this study by referring to the uncertainty ranges from CERES-derived product given by Kato et al. (2018) (Table 5), which indicates that all estimated energy components fall within these uncertainty ranges, except for the all-sky surface downward LW radiation, with about 3 W m^{-2} lower than the corresponding lowest CERES range. This is in line with its much higher CERES-derived estimate compared to that of the ERA5 (285 vs. 273 W m^{-2}) (Table 1).

Table 5. Uncertainties (Units: W m^{-2}) in 1°×1° regional monthly surface SW, LW, and net (SW + LW) fluxes under all-sky and clear-sky conditions for the CERES-EBAF Edition 4.1 product (referring to Kato et al. (2018)), as well as its corresponding estimates of various surface fluxes.

Uncertainties(1σ)	All-sky	Clear-sky
SW down	178±14	236±6
SW up	36±11	45±11
SW net	142±13	191±13
LW down	285±9	256±8
LW up	354±15	353±15
LW net	69±17	97±17
SW + LW net	73±20	95±20

Overall, around 21.6% and 56.9% of the TOA incoming solar radiation are absorbed by the atmosphere and surface, respectively, for clear-sky conditions, while these absorptions are 23.1% and 41.6% for all-sky conditions. This implies that the existence of clouds results in more atmospheric SW absorption of around 1.5% and much less surface solar absorption of around 15.3% with respect to the TOA incoming solar radiation.

5. The cloud radiative effects (CREs)

According to the annual land-mean best estimates of radiative components over East Asia under all-sky and clear-sky conditions obtained in previous sections, the present-day CREs can be inferred quantitively over this region. The calculated SW, LW, and net CREs at the TOA, within the atmosphere, and at the surface are therefore presented in Fig. 8. Moreover, the corresponding calculation formulas are also given in the followings:

$$\text{TOA SW CRE} = \text{TOA outgoing SW}_{\text{all-sky}} - \text{TOA outgoing SW}_{\text{clear-sky}}$$

$$\text{TOA LW CRE} = \text{TOA outgoing LW}_{\text{all-sky}} - \text{TOA outgoing LW}_{\text{clear-sky}}$$

546        $\text{TOA Net CRE} = \text{TOA SW CRE} + \text{TOA LW CRE}$

547

548        $\text{Surface Net SW CRE} = \text{Surface Net SW}_{\text{all-sky}} - \text{Surface Net SW}_{\text{clear-sky}}$

549        $\text{Surface Net LW CRE} = \text{Surface Net LW}_{\text{all-sky}} - \text{Surface Net LW}_{\text{clear-sky}}$

550        $\text{Surface Net total CRE} = \text{Surface Net SW CRE} + \text{Surface Net LW CRE}$

551

552        $\text{Atmospheric SW CRE} = \text{TOA SW CRE} - \text{Surface Net SW CRE}$

553        $\text{Atmospheric LW CRE} = \text{TOA LW CRE} - \text{Surface Net LW CRE}$

554
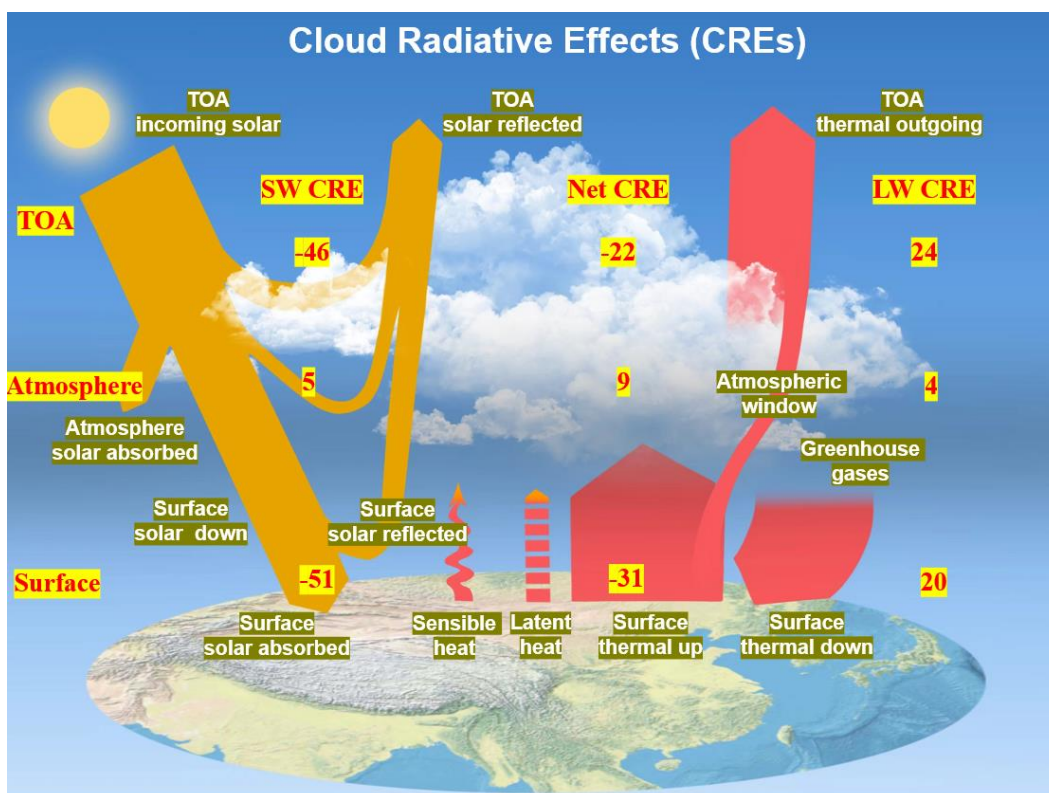
555

556   **Figure 8.** Diagram of the annual land mean SW, LW, and net (SW + LW) cloud radiative effects (CREs)
557   (Units: W m^{-2}) at the TOA, within the atmosphere, and at the surface over East Asia, calculated by the
558   differences between all-sky and clear-sky radiation budgets as given in Fig. 7.

559

560   Best estimates for the annual East Asian land-mean reflected solar radiation at the TOA under all-sky

561   and clear-sky conditions are -118 and -72 W m^{-2}, respectively, differing by -46 W m^{-2}, indicating that the

562   clouds give rise to an extra 46 W m^{-2} solar reflection at the TOA, thus cooling the Earth-atmosphere system.

563   Similarly, the TOA LW CRE, obtained as the difference between the TOA thermal radiation under all-sky

564   and clear-sky conditions, is 24 W m^{-2}, suggesting a warming effect of clouds on the system. Thus, the

565   estimated TOA net CRE is -22 W m^{-2}, pointing out that the overall effects of clouds result in an energy loss

566   and net cooling to the system, not only in the global mean, but also over East Asian land.

567   At the Earth's surface, the shading effects of clouds are estimated to reduce the surface solar radiation

568   by 60 W m^{-2}, from 234 to 174 W m^{-2}, while the surface solar absorption differs by 51 W m^{-2}, from 190 to

569   139 W m^{-2}, namely the surface net SW CRE is -51 W m^{-2}. On cloudy skies, the estimated surface downward

570   LW radiation increases from 253 to 273 W m^{-2}, with an increase of 20 W m^{-2}, illustrating that the surface

571   net LW CRE is 20 W m^{-2} and therefore leads to a surface warming. Thus, the surface net CRE, i.e., the sum

572   of the surface net SW and LW CRE, is then -31 W m^{-2}, indicating that clouds contribute more to the SW

573   energy budgets. Eventually, the clouds lead to the enhancement of the SW and LW absorption within the

574   atmosphere of around 5 and 4 W m^{-2}, respectively, thus resulting in an atmospheric net CRE of 9 W m^{-2} over

575   East Asian land.

576   The above CRE best estimates are compared with the corresponding estimates from different data

577   sources (Fig. 9; Table 1). Generally, compared to the LW CREs (Fig. 9b), the simulated SW CREs show

578   larger spreads and SDs amongst models (Fig. 9a; Table 1). For the SW CREs at the TOA, within the

579   atmosphere, and at the surface, the CERES-derived estimates match perfectly with the best estimates

580   mentioned above, within 2 W m^{-2} of the biases, followed by the estimates from the multi-model means and

581   ERA5 (Table 1). For the LW CREs, the calculated TOA LW CREs from the CMIP6 multi-model mean and

582   CERES differ by no more than 1 W m^{-2} compared to the best estimate, while large differences are noted at

583   the surface LW CREs, thereby leading to their opposite signs in the atmospheric LW CREs (Fig. 9b; Table

584   1). Specifically, since the ERA5-based TOA LW CRE deviates by no more than 3 W m^{-2} with the best

585   estimate of 24 W m^{-2} with nearly the same surface LW CRE, the estimated atmospheric LW CRE is therefore

586   the closest to the best estimate (Table 1). This is owing to the fact that we make use of the ERA5 data as the

587   reference to estimate the surface LW radiation. Thus, the major reason for the large discrepancies in the

588   atmospheric and surface LW CREs estimated from different data sources with respect to the best estimates

589   in this study is the determination of the surface downward and upward LW radiation, which is also the reason

590   for the large deviations in their net CREs (Fig. 9c).

591

592
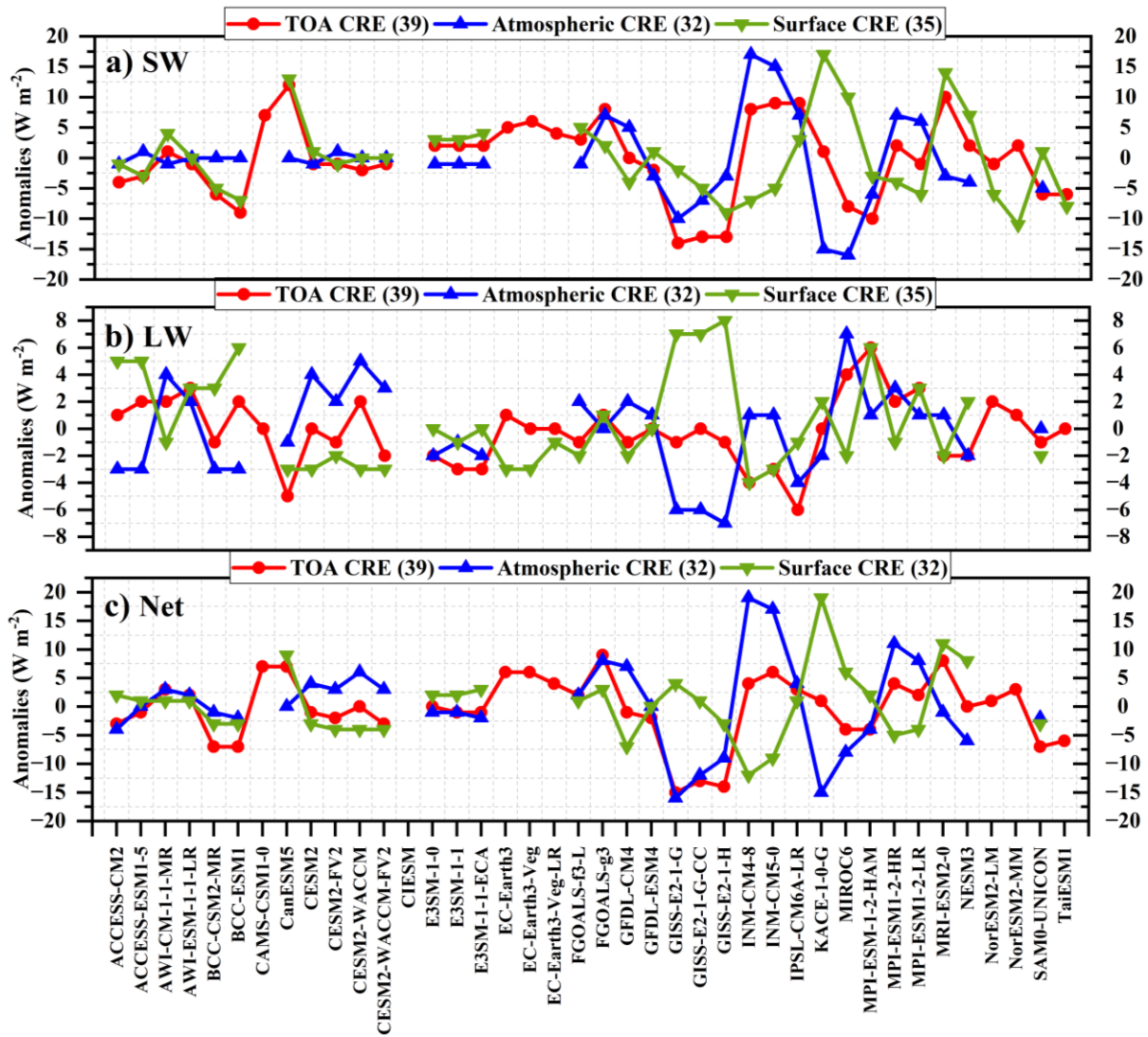
Figure 9. Annual land mean anomalies of (**a**) SW, (**b**) LW, and (**c**) net (SW + LW) CREs (Units: W m^{-2}) at the TOA (red line), within the atmosphere (blue line), and at the surface (green line) with regard to their respective multi-model means over East Asia, respectively, as represented by various CMIP6 models. The numbers in the parentheses indicate the available CMIP6 climate models for the corresponding radiation components.

598

A better comparison with the global annual mean best estimates of CREs by Wild et al. (2019) is given in Fig. S5. At the TOA, a slightly lower and much lower East Asian land-mean SW and LW CREs of 1 W m^{-2} and 4 W m^{-2} result in 3 W m^{-2} more energy loss at the TOA compared to the globe. At the surface, much lower annual East Asian land-mean SW and LW CREs by 3 W m^{-2} and 8 W m^{-2} are estimated compared to the values over the globe, leading to a net CRE deviation of 5 W m^{-2}, indicative of 5 W m^{-2} more energy loss at the surface. However, lower and higher annual East Asian land-mean SW and LW CREs of 2 and 4 W m^{-2} within the atmosphere contribute to the nearly close net CRE with a deviation of no more than 2 W m^{-2} compared to the global mean estimates. On the whole, lower annual East Asian land-mean best estimates in the absolute values of surface SW and LW CREs as well as the TOA LW CRE compared to their global mean counterparts give rise to the CRE differences between them.

6. Summary and conclusions

This study aims to explore how the energy budgets are interrupted by the complex orographic and thermal effects of the TP, as well as the high anthropogenic aerosol emissions over East Asian land compared to global land, based on complementary data sources from space and surface observations, as well as the CMIP6 climate models and ERA5 reanalysis. A further quantitative investigation of CREs at the TOA, within the atmosphere, and at the surface is also conducted.

Comparisons between all-sky and clear-sky energy budgets indicate that the overall effects of clouds greatly reduce the surface solar absorption by about 15.3% and enhance that within the atmosphere by 1.5%. Compared to the global land energy budget estimates from Wild et al. (2015), for the SW budgets, notably more atmospheric SW reflection of 5.2% but with a slightly less atmospheric SW absorption of 0.6% with respect to their respective TOA incident solar radiation are estimated over East Asian land, possibly indicating that the lower water vapor content effects due to TP overcompensate for the aerosol and cloud effects over East Asian land. For the LW budgets, a substantially lower surface LW emission of around 25 W m^{-2} and smaller relative surface downward LW radiation of around 3.6% with respect to their respective surface emissions can be noticed over East Asian land compared to global land, which possibly result from the lower regional surface skin temperature, as well as the weaker greenhouse effect and fewer low clouds mainly induced by the high altitude and thinner air over TP, thus leading to a higher percentage of regional OLR of 2.7%.

The CREs over East Asian land are inferred through the energy budget differences between all-sky and clear-sky conditions. The clouds reduce the solar absorption at the TOA by 46 W m^{-2} and enhance the TOA thermal radiation by 24 W m^{-2}, respectively, leading to a TOA net CRE of -22 W m^{-2}, a more cooling effect on the regional climate system than that over globe (-19 W m^{-2}). At the surface, the net CRE is estimated to be -31 W m^{-2} according to less solar absorption of 51 W m^{-2} and more downward thermal radiation of 20 W m^{-2}, indicative of larger cloud impacts on SW radiation. Within the atmosphere, the estimated net CRE is 9 W m^{-2} due to an increase of 5 W m^{-2} of solar absorption and 4 W m^{-2} of the net thermal radiation, respectively. Compared to the global mean best estimates of CREs as introduced by Wild et al. (2019), relatively lower East Asian land-mean best estimates of surface SW and LW CREs as well as the TOA LW CRE contribute to the CRE differences between them.

On the whole, all the estimated land-mean energy balance components over East Asia in this study fall within the uncertainty ranges of the CERES-derived assessments, except for the all-sky surface downward LW radiation. More accurate and reliable datasets should be utilized to reduce the substantial uncertainties in the regional energy balance estimates, particularly in the surface budgets, and more widespread temporal and spatial representations of energy budget research are recommended for more comprehensive comparisons in future. For example, newly published surface radiation products with high resolutions based on satellite datasets (e.g., Letu et al., 2022; Xu et al., 2022) are expected to make sense in improving the accuracy of the regional/global surface radiation budget studies.

645 *Acknowledgments.* This research was funded by the National Key Research and Development Program of

646 China (2017YFA0603502) and the Science and Technology Development Fund of CAMS

647 (2021KJ004&2022KJ019). The Global Energy Balance Archive (GEBA) is co-funded by the Federal

648 Office of Meteorology and Climatology Meteo Swiss within the framework of GCOS Switzerland.

649

650 *Data Availability.* The CERES SYN1deg data is available at https://ceres-tool.larc.nasa.gov/ord-

651 tool/jsp/SYN1degEd41Selection.jsp; The AIRS data is accessible from

652 https://disc.gsfc.nasa.gov/datasets/AIRS3STM_006/summary?keywords=AIRS; The MODIS data is from

653 https://ladsweb.modaps.eosdis.nasa.gov/archive/allData/61/MYD08_M3/?process=ftpAsHttp&path=allDat

654 a%2f61%2fMYD08_M3; The CloudSat data is from http://www.cloudsat.cira.colostate.edu/data-

655 products/level-2b/2b-cwc-ro; The MERRA-2 dataset is obtained at

656 https://disc.gsfc.nasa.gov/datasets/M2IMNPANA_5.12.4/summary?keywords=merra-2. The ERA-Interim

657 is from https://apps.ecmwf.int/datasets/data/interim-full-moda/levtype=sfc.

658

659 *Author contributions.* HZ, MW, and QW proposed the main ideas of this study. QW designed and wrote the

660 manuscript. SY provided the homogenized ground-based surface solar radiation data. QC, XZ, and GS

661 contributed to the interpretation of the results. BX and YW assisted with the figures. All co-authors

662 participated in discussions and provided constructive suggestions.

663

664 *Competing interests.* The authors declare that they have no conflict of interest.

665

References

667 Boeke, R. C., and Taylor, P. C.: Evaluation of the Arctic surface radiation budget in CMIP5 models, J. Geophys.
668   Res.-Atmos., 121, 8525–8548, https://doi.org/10.1002/2016JD025099, 2016.

669 Christensen, M. W., Behrangi, A., L'Ecuyer, T. S., Wood, N. B., Lebsock, M. D., and Stephens, G. L.: Arctic
670   observation and reanalysis integrated system: A new data product for validation and climate study, B. Am.
671   Meteorol. Soc., 97, 907–916, https://doi.org/10.1175/BAMS-D-14-00273.1, 2016.

672 de Leeuw, G., Sogacheva, L., Rodriguez, E., Kourtidis, K., Georgoulias, A. K., Alexandri, G., Amiridis, V.,
673   Proestakis, E., Marinou, E., Xue, Y., and van der A, R.: Two decades of satellite observations of AOD over
674   mainland China using ATSR-2, AATSR and MODIS/Terra: data set evaluation and large-scale patterns, Atmos.
675   Chem. Phys., 18, 1573–1592, https://doi.org/10.5194/acp-18-1573-2018, 2018.

676 Dolinar, E. K., Dong, X., Xi, B., Jiang, J. H., and Su, H.: Evaluation of CMIP5 simulated clouds and TOA
677   radiation budgets using NASA satellite observations, Clim. Dynam., 44, 2229–2247,
678   https://doi.org/10.1007/s00382-014-2158-9, 2015.

679 Eyring, V., Bony, S., Meehl, G. A., Senior, C. A., Stevens, B., Stouffer, R. J., and Taylor, K. E.: Overview of the
680   Coupled Model Intercomparison Project Phase 6 (CMIP6) experimental design and organization, Geosci.
681   Model Dev., 9, 1937–1958, https://doi.org/10.5194/gmd-9-1937-2016, 2016.

682 Fan, T., Zhao, C., Dong, X., Liu, X., Yang, X., Zhang, F., Shi, C., Wang, Y., and Wu, F.: Quantify contribution
683   of aerosol errors to cloud fraction biases in CMIP5 Atmospheric Model Intercomparison Project simulations,
684   Int. J. Climatol., 38, 3140–3156, https://doi.org/10.1002/joc.5490, 2018.

685 Fasullo, J. T., and Trenberth, K. E.: The annual cycle of the energy budget. Part I: Global mean and land-ocean
686   exchanges, J. Climate, 21, 2297–2312, https://doi.org/10.1175/2007JCLI1935.1, 2008a.

687 Fasullo, J. T., and Trenberth, K. E.: The annual cycle of the energy budget. Part II: Meridional structures and
688   poleward transports, J. Climate, 21, 2313–2325, https://doi.org/10.1175/2007JCLI1936.1, 2008b.

689 Ghan, S. J., Liu, X., Easter, R. C., Zaveri, R., Rasch, P. J., Yoon, J.-H, and Eaton, B.: Toward a minimal

690   representation of aerosols in climate models: Comparative decomposition of aerosol direct, semidirect, and
691   indirect radiative forcing, J. Climate, 25, 6461-6476, https://doi.org/10.1175/JCLI-D-11-00650.1, 2012.
692 Gilgen, H., Wild, M., and Ohmura, A.: Means and trends of shortwave irradiance at the surface estimated from
693   global energy balance archive data, J. Climate, 11, 2042–2061, https://doi.org/10.1175/1520-
694   0442(1998)011<2042:MATOSI>2.0.CO;2, 1998.
695 He, Y., Wang, K., Zhou, C., and Wild, M.: A revisit of global dimming and brightening based on the sunshine
696   duration, Geophys. Res. Lett., 45, 4281–4289, https://doi.org/10.1029/2018GL077424, 2018.
697 Hersbach, H., Bell, B., Berrisford, P., Hirahara, S., Horányi, A., Muñoz-Sabater, J., Nicolas, J., Peubey, C., Radu,
698   R., Schepers, D., Simmons, A., Soci, C., Abdalla, S., Abellan, X., Balsamo, G., Bechtold, P., Biavati, G., Bidlot,
699   J., Bonavita, M., De Chiara, G., Dahlgren, P., Dee, D., Diamantakis, M., Dragani, R., Flemming, J., Forbes,
700   R., Fuentes, M., Geer, A., Haimberger, L., Healy, S., Hogan, R. J., Hólm, E., Janisková, M., Keeley, S.,
701   Laloyaux, P., Lopez, P., Lupu, C., Radnoti, G., de Rosnay, P., Rozum, I., Vamborg, F., Villaume, S., and
702   Thépaut, J.: The ERA5 global reanalysis, Q. J. Roy. Meteor. Soc., 146, 1999–2049,
703   https://doi.org/10.1002/qj.3803, 2020.
704 Huang, G., Li, Z., Li, X., Liang, S., Yang, K., Wang, D., and Zhang, Y.: Estimating surface solar irradiance from
705   satellites: Past, present, and future perspectives, Remote Sens. Environ., 233, 111371,
706   https://doi.org/10.1016/j.rse.2019.111371, 2019.
707 Kato, S., Rose, F. G., Rutan, D. A., Thorsen, T. J., Loeb, N. G., Doelling, D. R., Huang, X., Smith, W. L., Su, W.,
708   and Ham, S.: Surface Irradiances of Edition 4.0 Clouds and the Earth's Radiant Energy System (CERES)
709   Energy Balanced and Filled (EBAF) data product, J. Climate, 31, 4501–4527, https://doi.org/10.1175/JCLI-D-
710   17-0523.1, 2018.
711 Kim, B., and Lee, K.: Radiation component calculation and energy budget snalysis for the Korean Peninsula
712   region, Remote Sens., 10, 1147, https://doi.org/10.3390/rs10071147, 2018.
713 King, M. D., Platnick, S., Menzel, W. P., Ackerman, S. A., and Hubanks, P. A.: Spatial and temporal distribution
714   of clouds observed by MODIS onboard the Terra and Aqua satellites, IEEE T. Geosci. Remote Sens., 51, 3826–
715   3852, https://doi.org/10.1109/TGRS.2012.2227333, 2013.
716 L'Ecuyer, T. S., Beaudoing, H. K., Rodell, M., Olson, W., Lin, B., Kato, S., Clayson, C. A., Wood, E., Sheffield,
717   J., Adler, R., Huffman, G., Bosilovich, M., Gu, G., Robertson, F., Houser, P. R., Chambers, D., Famiglietti, J.
718   S., Fetzer, E., Liu, W. T., Gao, X., Schlosser, C. A., Clark, E., Lettenmaier, D. P., and Hilburn, K.: The observed
719   state of the energy budget in the early twenty-First century, J. Climate, 28, 8319–8346,
720   https://doi.org/10.1175/JCLI-D-14-00556.1, 2015.
721 Lei, Y., Letu, H., Shang, H., and Shi, J.: Cloud cover over the Tibetan Plateau and eastern China: a comparison
722   of ERA5 and ERA-Interim with satellite observations, Clim. Dynam., 54, 2941–2957,
723   https://doi.org/10.1007/s00382-020-05149-x, 2020.
724 Letu, H., Nakajima, T.Y., Wang, T., Shang, H., Ma, R., Yang, K., Baran, A.J., Riedi, J., Ishimoto, H., and Yoshida,
725   M.: A new benchmark for surface radiation products over the East Asia−Pacific region retrieved from the
726   Himawari-8/AHI next-generation geostationary satellite, B. Am. Meteorol. Soc., 103, E873-E888,
727   https://doi.org/10.1175/BAMS-D-20-0148.1, 2022.
728 Li, J. -L. F., Waliser, D. E., Stephens, G., Lee, S., L'Ecuyer, T., Kato, S., Loeb, N., and Ma, H.: Characterizing
729   and understanding radiation budget biases in CMIP3/CMIP5 GCMs, contemporary GCM, and reanalysis, J.
730   Geophys. Res.-Atmos., 118, 8166–8184, https://doi.org/10.1002/jgrd.50378, 2013.
731 Li, J., and Mao, J.: A preliminary evaluation of global and East Asian cloud radiative effects in reanalyses, Atmos.
732   and Ocean. Sci. Lett., 8, 100-106, https://doi.org/10.3878/AOSL20140093, 2015.
733 Li, J., Mao, J., and Wang, F.: Comparative study of five current reanalyses in characterizing total cloud fraction
734   and top-of-the-atmosphere cloud radiative effects over the Asian monsoon region, Int. J. Climatol., 37, 5047–
735   5067, https://doi.org/10.1002/joc.5143, 2017.
736 Li, Z., Niu, F., Fan, J., Liu, Y., Rosenfeld, D., and Ding, Y.: Long-term impacts of aerosols on the vertical
737   development of clouds and precipitation, Nat. Geosci., 4, 888-894, https://doi.org/10.1038/ngeo1313, 2011.
738 Liao, H., Chang, W., and Yang, Y.: Climatic effects of air pollutants over china: A review, Adv. Atmos. Sci., 32,
739   115–139, https://doi.org/10.1007/s00376-014-0013-x, 2015.
740 Lin, B., Stackhouse Jr., P. W., Minnis, P., Wielicki, B. A., Hu, Y., Sun, W., Fan, T., and Hinkelman, L. M.:
741   Assessment of global annual atmospheric energy balance from satellite observations, J. Geophys. Res.-Atmos.,
742   113, https://doi.org/10.1029/2008JD009869, 2008.
743 Liu, Y., Bao, Q., Duan, A., Qian, Z. A., and Wu, G.: Recent progress in the impact of the Tibetan Plateau on
744   climate in China, Adv. Atmos. Sci., 24, 1060–1076, https://doi.org/10.1007/s00376-007-1060-3, 2007.
745 Loeb, N. G., Doelling, D. R., Wang, H., Su, W., Nguyen, C., Corbett, J. G., Liang, L., Mitrescu, C., Rose, F. G.,
746   and Kato, S.: Clouds and the Earth's Radiant Energy System (CERES) Energy Balanced and Filled (EBAF)
747   Top-of-Atmosphere (TOA) Edition-4.0 data product, J. Climate, 31, 895–918, https://doi.org/10.1175/JCLI-
748   D-17-0208.1, 2018.

Mayer, M., Tietsche, S., Haimberger, L., Tsubouchi, T., Mayer, J., and Zuo, H.: An improved estimate of the coupled Arctic energy budget, J. Climate, 32, 7915–7934, https://doi.org/10.1175/JCLI-D-19-0233.1, 2019.

Mercado, L. M., Bellouin, N., Sitch, S., Boucher, O., Huntingford, C., Wild, M., and Cox, P. M.: Impact of changes in diffuse radiation on the global land carbon sink, Nature, 458, 1014–1017, https://doi.org/10.1038/nature07949, 2009.

Ohmura, A.: Cryosphere During the Twentieth Century, The state of the planet: frontiers and challenges in geophysics, Geophys. Monogr. Ser., 150, 239–257, https:// doi.org/10.1029/150gm19, 2004.

Previdi, M., Smith, K. L., and Polvani, L. M.: How well do the CMIP5 models simulate the Antarctic atmospheric energy budget? J. Climate, 28, 7933–7942, https://doi.org/10.1175/JCLI-D-15-0027.1, 2015.

Raschke, E., Kinne, S., Rossow, W. B., Stackhouse, P. W., and Wild, M.: Comparison of radiative energy flows in observational datasets and climate modeling, J. Appl. Meteorol. Clim., 55, 93–117, https://doi.org/10.1175/JAMC-D-14-0281.1, 2016.

Simmons, A. J., Jones, P. D., Da Costa Bechtold, V., Beljaars, A. C. M., Kållberg, P. W., Saarinen, S., Uppala, S. M., Viterbo, P., and Wedi, N.: Comparison of trends and low-frequency variability in CRU, ERA-40, and NCEP/NCAR analyses of surface air temperature, J. Geophys. Res.-Atmos., 109, https://doi.org/10.1029/2004JD005306, 2004.

Stephens, G. L.: Cloud feedbacks in the climate system: A critical review, J. Climate, 18, 237-273, https://doi.org/10.1175/JCLI-3243.1, 2005.

Stephens, G. L., Li, J., Wild, M., Clayson, C. A., Loeb, N., Kato, S., L'Ecuyer, T., Stackhouse, P. W., Lebsock, M., and Andrews, T.: An update on Earth's energy balance in light of the latest global observations, Nat. Geosci., 5, 691–696, https://doi.org/10.1038/ngeo1580, 2012.

Tang, W. J., Qin, J., Yang, K., Zhu, F., and Zhou, X.: Does ERA5 outperform satellite products in estimating atmospheric downward longwave radiation at the surface? Atmos. Res., 252, 105453, https://doi.org/10.1016/j.atmosres.2021.105453, 2021.

Tang, W. J., Yang, K., Qin, J., Cheng, C. C. K., and He, J.: Solar radiation trend across China in recent decades: a revisit with quality-controlled data, Atmos. Chem. Phys., 11, 393–406, https://doi.org/10.5194/acp-11-393-2011, 2011.

Thomas, C. M., Dong, B., and Haines, K.: Inverse modeling of global and regional energy and water cycle fluxes using earth observation data, J. Climate, 33, 1707–1723, https://doi.org/10.1175/JCLI-D-19-0343.1, 2020.

Trenberth, K. E., Fasullo, J. T., and Balmaseda, M. A.: Earth's energy imbalance, J. Climate, 27, 3129–3144, https://doi.org/10.1175/JCLI-D-13-00294.1, 2014.

Trenberth, K. E., Fasullo, J. T., and Kiehl, J.: Earth's global energy budget, B. Am. Meteorol. Soc., 90, 311–324, https://doi.org/10.1175/2008BAMS2634.1, 2009.

Trolliet, M., Walawender, J. P., Bourlès, B., Boilley, A., Trentmann, J., Blanc, P., Lefèvre, M., and Wald, L.: Downwelling surface solar irradiance in the tropical Atlantic Ocean: a comparison of re-analyses and satellite-derived data sets to PIRATA measurements, Ocean Sci., 14, 1021–1056, https://doi.org/10.5194/os-14-1021-2018, 2018.

Urraca, R., Huld, T., Gracia-Amillo, A., Martinez-de-Pison, F. J., Kaspar, F., and Sanz-Garcia, A.: Evaluation of global horizontal irradiance estimates from ERA5 and COSMO-REA6 reanalyses using ground and satellite-based data, Sol. Energy, 164, 339–354, https://doi.org/10.1016/j.solener.2018.02.059, 2018.

Wang, H., Zhang, H., Xie, B., Jing, X., He, J., and Liu, Y.: Evaluating the Impacts of Cloud Microphysical and Overlap Parameters on Simulated Clouds in Global Climate Models, Adv. Atmos. Sci., https://doi.org/10.1007/s00376-021-0369-7, 2021.

Wang, K.: Measurement biases explain discrepancies between the observed and simulated decadal variability of surface incident solar radiation, Sci. Rep., 4, 6144, https://doi.org/10.1038/srep06144, 2014.

Wang, K., Ma, Q., Li, Z., and Wang, J.: Decadal variability of surface incident solar radiation over China: Observations, satellite retrievals, and reanalyses, J. Geophys. Res.-Atmos., 120, 6500–6514, https://doi.org/10.1002/2015JD023420, 2015.

Wang, Q., Zhang, H., Yang, S., Chen, Q., Zhou, X., Shi, G., Cheng, Y., and Wild, M.: Potential driving factors on surface solar radiation trends over China in recent years, Remote Sens., 13, 704, https://doi.org/10.3390/rs13040704, 2021.

Wang, Y., Trentmann, J., Yuan, W., and Wild, M.: Validation of CM SAF CLARA-A2 and SARAH-E surface solar radiation datasets over China, Remote Sens., 10, 1977, https://doi.org/10.3390/rs10121977, 2018.

Wang, Y., Wild, M., Sanchez-Lorenzo, A., and Manara, V.: Urbanization effect on trends in sunshine duration in China, Ann. Geophys., 35, 839–851, https://doi.org/10.5194/angeo-35-839-2017, 2017.

Wang, Y., and Wild, M.: A new look at solar dimming and brightening in China, Geophys. Res. Lett., 43, 11, 711–777, 785, https://doi.org/10.1002/2016GL071009, 2016.

Wang, Z., Lin, L., Xu, Y., Che, H., Zhang, X., Zhang, H., Dong, W., Wang, C., Gui, K., and Xie, B.: Incorrect Asian aerosols affecting the attribution and projection of regional climate change in CMIP6 models, npj Clim.

808   Atmos. Sci., 4, 1–8, https://doi.org/10.1038/s41612-020-00159-2, 2021.

809 Wei, J., Peng, Y., Guo, J., and Sun, L.: Performance of MODIS Collection 6.1 Level 3 aerosol products in spatial-
810   temporal variations over land, Atmos. Environ., 206, 30–44, https://doi.org/10.1016/j.atmosenv.2019.03.001,
811   2019.

812 Wild, M.: Progress and challenges in the estimation of the global energy balance, AIP Conference Proceedings,
813   1810, 20004, https://doi.org/10.1063/1.4975500, 2017a.

814 Wild, M.: Towards global estimates of the surface energy budget, Curr. Clim. Change Rep., 3, 87–97,
815   https://doi.org/10.1007/s40641-017-0058-x, 2017b.

816 Wild, M.: The global energy balance as represented in CMIP6 climate models, Clim. Dynam., 55, 553–577,
817   https://doi.org/10.1007/s00382-020-05282-7, 2020.

818 Wild, M., Folini, D., Hakuba, M. Z., Schär, C., Seneviratne, S. I., Kato, S., Rutan, D., Ammann, C., Wood, E. F.,
819   and König-Langlo, G.: The energy balance over land and oceans: an assessment based on direct observations
820   and CMIP5 climate models, Clim. Dynam., 44, 3393–3429, https://doi.org/10.1007/s00382-014-2430-z, 2015.

821 Wild, M., Folini, D., Schär, C., Loeb, N., Dutton, E. G., and König-Langlo, G.: The global energy balance from
822   a surface perspective, Clim. Dynam., 40, 3107–3134, https://doi.org/10.1007/s00382-012-1569-8, 2013a.

823 Wild, M., Folini, D., Schär, C., Loeb, N., Dutton, E. G., and König-Langlo, G.: A new diagram of the global
824   energy balance, AIP Conference Proceedings, 1531, 628–631, https://doi.org/10.1063/1.4804848, 2013b.

825 Wild, M., Grieser, J., and Schär, C.: Combined surface solar brightening and increasing greenhouse effect support
826   recent intensification of the global land-based hydrological cycle, Geophys. Res. Lett., 35,
827   https://doi.org/10.1029/2008GL034842, 2008.

828 Wild, M., Hakuba, M. Z., Folini, D., Dörig-Ott, P., Schär, C., Kato, S., and Long, C. N.: The cloud-free global
829   energy balance and inferred cloud radiative effects: an assessment based on direct observations and climate
830   models, Clim. Dynam., 52, 4787–4812, https://doi.org/10.1007/s00382-018-4413-y, 2019.

831 Wild, M., Hakuba, M. Z., Folini, D., Schär, C., and Long, C.: New estimates of the Earth radiation budget under
832   cloud-free conditions and cloud radiative effects, AIP Conference Proceedings, 1810, 90012,
833   https://doi.org/10.1063/1.4975552, 2017.

834 Wild, M., Ohmura, A., Gilgen, H., and Roeckner, E.: Validation of general circulation model radiative fluxes
835   using surface observations, J. Climate, 8, 1309–1324, https://doi.org/10.1175/1520-
836   0442(1995)008<1309:VOGCMR>2.0.CO;2, 1995.

837 Wu, G., Duan, A., Liu, Y., Mao, J., Ren, R., Bao, Q., He, B., Liu, B., and Hu, W.: Tibetan Plateau climate
838   dynamics: recent research progress and outlook, Natl. Sci. Rev., 2, 100–116,
839   https://doi.org/10.1093/nsr/nwu045, 2015.

840 Xu, J., Liang, S., and Jiang, B.: A global long-term (1981−2019) daily land surface radiation budget product from
841   AVHRR satellite data using a residual convolutional neural network, Earth Syst. Sci. Data, 14, 2315-2341,
842   https://doi.org/10.5194/essd-14-2315-2022, 2022.

843 Xu, X., Lu, C., Shi, X., and Gao, S.: World water tower: An atmospheric perspective, Geophys. Res. Lett., 35,
844   https://doi.org/10.1029/2008GL035867, 2008a.

845 Xu, X., Zhang, R., Koike, T., Lu, C., Shi, X., Zhang, S., Bian, L., Cheng, X., Li, P., and Ding, G.: A new integrated
846   observational system over the Tibetan Plateau, B. Am. Meteorol. Soc., 89, 1492–1496, 2008b.

847 Yang, S., Wang, X. L., and Wild, M.: Homogenization and trend analysis of the 1958−2016 in situ surface solar
848   radiation records in China, J. Climate, 31, 4529–4541, https://doi.org/10.1175/JCLI-D-17-0891.1, 2018.

849 Yang, S., Wang, X. L., and Wild, M.: Causes of dimming and brightening in China inferred from homogenized
850   daily clear-sky and all-sky in situ surface solar radiation records (1958–2016), J. Climate, 32, 5901–5913,
851   https://doi.org/10.1175/JCLI-D-18-0666.1, 2019.

852 You, Q., Liu, J., and Pepin, N.: Changes of summer cloud water content in China from ERA-Interim reanalysis,
853   Global Planet. Change, 175, 201–210, https://doi.org/10.1016/j.gloplacha.2019.02.014, 2019.

854 Zhang, H., Zhao, M., Chen, Q., Wang, Q., Zhao, S., Zhou, X., and Peng, J.: Water and ice cloud optical thickness
855   changes and radiative effects in East Asia, J. Quant. Spectrosc. Radiat. Transf., 254, 107213,
856   https://doi.org/10.1016/j.jqsrt.2020.107213, 2020.